ISTANBUL TECHNICAL UNIVERSITY ★ GRADUATE SCHOOL OF SCIENCE ENGINEERING AND TECHNOLOGY

PICO SATELLITE ATTITUDE AND ATTITUDE RATE ESTIMATION USING KALMAN FILTERING

M.Sc. THESIS

Yeliz SAKA YILDIZ

Department of Aeronautics and Astronautics Engineering

Aeronautics and Astronautics Engineering Programme

MAY 2020

ISTANBUL TECHNICAL UNIVERSITY ★ GRADUATE SCHOOL OF SCIENCE ENGINEERING AND TECHNOLOGY

PICO SATELLITE ATTITUDE AND ATTITUDE RATE ESTIMATION USING KALMAN FILTERING

M.Sc. THESIS

Yeliz SAKA YILDIZ
(511161188)

Department of Aeronautics and Astronautics Engineering

Aeronautics and Astronautics Engineering Programme

Thesis Advisor: Prof. Dr. Cengiz HACIZADE

MAY 2020

İSTANBUL TEKNİK ÜNİVERSİTESİ ★ FEN BİLİMLERİ ENSTİTÜSÜ

KALMAN FİLTRESİ KULLANILARAK PICO UYDU YÖNELİM VE YÖNELİM ORANI BELİRLEME

YÜKSEK LİSANS TEZİ

Yeliz SAKA YILDIZ
(511161188)

Uçak ve Uzay Mühendisliği Anabilim Dalı

Uçak ve Uzay Mühendisliği Programı

Tez Danışmanı: Prof. Dr. Cengiz HACIZADE

MAYIS 2020

Yeliz SAKA YILDIZ, a M.Sc. student of ITU Graduate School of Science Engineering and Technology 511161188 successfully defended the thesis entitled "PICO SATELLITE ATTITUDE AND ATTITUDE RATE ESTIMATION USING KALMAN FILTERING", which she prepared after fulfilling the requirements specified in the associated legislations, before the jury whose signatures are below.

Thesis Advisor :	**Prof. Dr. Cengiz HACIZADE** Istanbul Technical University	.....
Jury Members :	**Prof. Dr. Fikret ÇALIŞKAN** Istanbul Technical University	.....
	Assist. Prof. Dr. Janset DAŞDEMİR Yıldız Technical University	.....

Date of Submission : **4 May 2020**
Date of Defense : **29 May 2020**

To my spouse and family,

FOREWORD

I would like to thank my advisor Prof. Dr. Cengiz Hacızade for his precious guidance, advice throughout my graduate studies and valuable contributions. He introduced me to fault tolerant systems and provided me with assistance whenever it was needed. I would like to thank my family for always being there and supporting me not only physically but also emotionally. A special parenthesis goes for my husband Dr. Kaan Yıldız for believing in me and helping me out whenever I face an obstacle.

May 2020 Yeliz SAKA YILDIZ

TABLE OF CONTENTS

Page

ABBREVIATIONS

AD : Attitude Determination
ARES : Attitude Rate Estimation
ECI : Earth Centered Inertial
EKF : Extended Kalman Filter
FDI : Fault Determination Isolation
JD : Julian Date
LEO : Low Earth Orbit
MNSF : Measurement Noise Scale Factor
MSE : Mean Square Error
REKF : Robust Extended Kalman Filter
TAM : Three Axis Magnetometer
TRIAD : Three Axis Attitude Determination

SYMBOLS

$\mathbf{A}$	: Direction cosine matrix
$\mathbf{b}$	: Body measurement vector
$\mathbf{e}$	: Residual
$\mathbf{H}$	: Magnetic field vector
$\mathbf{i}$	: Orbit inclination
$\mathbf{J}$	: Inertia matrix
$\mathbf{K}$	: Kalman gain
$\mathbf{M_e}$	: Magnetic dipole moment of the Earth
$\mathbf{M_{Sun}}$	: Mean anomaly of the Sun
$\mathbf{N_T}$	: Disturbance torque vector
$\mathbf{n}$	: Noise
$\mathbf{P}$	: Attitude covariance matrix
$\mathbf{r}$	: Orbit radius
$\mathbf{S}$	: Measurement noise scale factor
$\mathbf{s}$	: Sun direction vector
$\mathbf{T}$	: Transformation matrix
$\mathbf{v}$	: Measurement noise vector
$\mathbf{x}$	: State vector
β	: Statistical function
$\Delta_\mathbf{t}$	: Time step
δ	: Kronecker symbol
ε	: Magnetic dipole tilt
θ	: Pitch angle
$\lambda_{\mathbf{ecliptic}}$	: Ecliptic longitude
$\lambda_{\mathbf{M_{Sun}}}$	: Mean longitude of the Sun
μ	: Earth gravitational constant
σ	: Standard deviation
ϕ	: Roll angle
χ^2	: Chi-square value
ψ	: Yaw angle
$\omega_\mathbf{e}$	: Spin rate of the Earth

LIST OF TABLES

Page

LIST OF FIGURES

Page

PICO SATELLITE ATTITUDE AND ATTITUDE RATE ESTIMATION USING KALMAN FILTERING

SUMMARY

One of the most commonly encountered critical problems in spacecraft navigation is the computational burden during attitude determination. Another problem can be defined as a faulty or malfunctioning onboard sensor during the space mission. When it comes to small satellites that are not designed to carry high-performance computers to the space, difficulties in efficient data processing and computation may arise which could be resolved via ground stations. The information processed on Earth are then transmitted to the spacecraft to achieve satisfactory control over the vehicle. However, in the case of a malfunctioning receiver, it is highly crucial to compensate it for the sake of the mission.

In this work, static attitude determination methods were investigated to alleviate the computation burden. For this purpose, two approaches which use the data obtained from magnetometer and sun sensor were presented to estimate the attitude angles and angular velocities. Additionally, covariance analyses were conducted for the corresponding methods. Since, these vector-based methods have low accuracy while ensuring fast computation, they were implemented into one of the most common attitude determination methods, Extended Kalman Filter (EKF). The attitude angle, angular velocity estimations and their covariances were obtained by TRIAD and ARES approaches, and the outputs were employed in the EKF as measurement model. By doing so, the applied non-traditional approach of EKF was linearized in terms of the measurement models. The results of EKF and non-traditional EKF were compared and presented. The traditional EKF approach was succeed more accurate results than the non-traditional EKF.

Furthermore, a Robust Extended Kalman Filter (REKF) technique was introduced in case of a existing faulty sensor within the system. This method includes the detection and isolation of the failures in sensors. In this way, it is possible determine which sensors are malfunctioning. Regarding the working principle of the algorithm, in a presence of a fault in the measurement sensors, the EKF behaves as REKF, otherwise it proceeds normally. As a result, the attitude angles and the angular velocities used to achieve attitude determination were simulated autonomously with presence of a fault and satisfying results are obtained. Simulation results showed that if a perpetual fault was defined to the system, it led to accumulation and the algorithm was not found to be robust enough to eliminate it. However, if the fault was given within a certain time interval, then the REKF scheme was found to be working successfully with an acceptable accuracy. As future work, the aim is to extend this study by diagnosing the fault and achieving its recovery.

KALMAN FİLTRESİ KULLANILARAK PICO UYDU YÖNELİM VE YÖNELİM ORANI BELİRLEME

ÖZET

Geçmişte yaşanılan kazalar uzay görevlerini tek bir uzay aracı üzerinden tasarlamanın risklerini gözler önüne sermiştir. Neyse ki gelişen kontrol yöntemleri tek bir büyük uydu yerine belli bir sayıda küçük uydu kümesinin uzay görevlerinde kullanılmasına olanak sağlamıştır. Özellikle düşük irtifalı yörünge görevlerinde, çoğunlukla takım veya sürü olarak adlandırılan, birden fazla küçük uydunun bir uzay görevini gerçekleştirmesi senaryosu ile görev tasarımları gerçekleştirilmiş ve bu görevler başarıyla sonuçlanmışlardır. Bu tarz görevlerde çokça tercih edilen piko-uydular, küçük uydular sınıfının bir alt üyesidir. Faydalı yük olarak çeşitli bilimsel deney düzenekleri veya mühendislik gereçleri taşıyan bu uydular, maksimum 1 kg ağırlığında üretilmektedir. Uydunun görece küçük olan boyutları göz önünde bulundurulduğunda, uzay görevi için hayati öneme sahip alt sistemlerden biri olan yönelim belirleme ve kontrol sistemi kısıtlı hacme uyum sağlamak üzere geliştirilmiştir. Bu doğrultuda, yönelim belirleme donanım aracı olarak çoğunlukla, hafiflik, güvenilirlik, düşük güç tüketimi ihtiyacı özelliklerine sahip olan manyetometre ve güneş sensörü tercih edilmektedir.

Piko-uyduların seyrüseferi sırasında karşılaşılan en büyük problemlerden birisi, yönelim belirleme esnasında yürütülen hesaplama işleminin gereğinden uzun sürmesidir. Bir diğer problem ise sefer sırasında hatalı çalışan bir sensörün ortaya çıkması ya da çeşitli sebeplerle bozulmasıdır. Piko-uydular boyutları ve güç bütçeleri göz önüne alındığında yüksek performansa sahip bilgisayarlar taşımak yerine, faydalı yükü daha uygun bir şekilde kullanmak amacıyla, genellikle yer istasyonlarında yapılan veri işlemeleri, hesaplamalar ve bu hesaplamaların uzay araçlarına gönderilmeleri ile kontrol edilirler. Ancak eğer uyduya gönderilen radyo sinyalini alacak sensörde bir arıza mevcut ise bunu telafi etmek görevin başarısı için hayati önem taşımaktadır.

Bu çalışmada, durum vektörü Euler açıları ve bu açıların açısal hızları olmak üzere 6 serbestlik derecesi ile oluşturulmuştur. Ek olarak, yönelim kestirimi için uygulanacak yöntemlerde kullanılacak ölçüm sensörleri, manyetometre ve güneş sensörü olarak seçilmiştir. Piko-uyduların yönelim kestiriminde en çok tercih edilen yöntemlerden biri olan genişletilmiş Kalman filtresi, uydu yüksek hızda dönerken verimli sonuç vermemektedir. Bu yüzden, ağır hesaplama yükünden kurtulmak ve uydu yüksek hızda dönerken dahi yönelim kestirimini gerçekleştirebilmek için ilk olarak statik yönelim belirleme yöntemleri incelenmiştir. Bu doğrultuda, yönelim açılarının ve açısal hızlarının kestirimi için iki farklı yaklaşım izlenmiştir. Vektör esaslı yöntemlerden ilki, yönelim açılarının kestirimi için kullanılan iki vektör algoritmasıdır (TRIAD). İki vektör algoritması, yalnızca cebirsel işlem uygulanarak gerçekleştirilir. İkinci yöntem ise, açısal hızların kestirimi için kullanılan en küçük kareler yöntemi (ARES) yaklaşımıyla oluşturulmuş iteratif bir yöntemdir. Gerçekleştirilen simülasyonlarda, bu

yöntemin doğruluk ölçütünün, ölçüm modeli olarak kullanılan sensörlerin doğruluk seviyeleri ile doğrudan ilişkili olduğu görülmüştür. Yönelim kestirimine ek olarak, belirtilen yöntemlerin kovaryans analizleri de gerçekleştirilmiştir.

Vektör esaslı yöntemler yüksek hızlı hesaplama sağlamalarına rağmen düşük doğruluk seviyesine sahiptirler. Bu nedenle, vektör esaslı yöntemler en yaygın kullanılan yönelim belirleme yöntemlerinden biri olan genişletilmiş Kalman filtresine entegre edilmiştir. Ortaya çıkan bu yeni yöntem ile yönelim açıları, açısal hızları ve bunların kovaryansları iki vektör algoritması ve en küçük kareler yöntemi yaklaşımları kullanılarak elde edilmiştir. Elde edilen çıktılar Kalman filtresine ölçüm modeli olarak beslenmiştir. Mevcut durumda ölçüm modeli lineer hale getirilmiş olup, bu yöntem geleneksel olmayan genişletilmiş Kalman filtresi olarak ifade edilmiştir. Ölçüm modelleri çeşitli varyasyonlarla oluşturularak farklı yönelim kestirim yöntemleri elde edilmiştir. Bu yöntemlerin herbiri simüle edilmiş ve çıktıları hataların ortalamasının karekökü üzerinden karşılaştırılmıştır. Bu sonuçlara göre, geleneksel genişletilmiş Kalman filtresi yaklaşımının geleneksel olmayan genişletilmiş Kalman filtresinden daha büyük doğrulukla sonuç verdiği görülmüştür.

İlgilenilen bir diğer problemde, manyetometre sensöründe oluşabilecek bir hata senaryosu yaratılmıştır. Genişletilmiş Kalman filtresi kullanılan senaryoda, manyetometre modeline doğrudan kayma eklenerek veya manyetometrenin gürültü vektörü bir sabit ile çarpılarak sisteme belli bir iterasyon aralığında hata tanımlanmıştır. Bu durumda gerçekleştirilen simülasyonda, genişletilmiş Kalman filtresinin yönelim kestirimini yüksek hata payı ile gerçekleştirdiği gösterilmiştir. Hata payını kabul edilebilir bir sınıra çekmek için genişletilmiş Kalman filtresine bir iyileştirme çalışması yapılmıştır. Burada belirtilen çalışma, sensörde meydana gelebilecek olası bir hatanın tespit edilmesini ve ayrıştırılmasını ve hatanın elimine edilmesini içermektedir. Genişletilmiş Kalman filtresinin doğası gereği hesapladığı, tahmin edilen durum vektöründeki artık kullanılarak gözetleme istatistiği oluşturulmuştur. Gözetleme istatistiği, bir diğer deyişle chi-kare testi, her bir iterasyon adımında sistemin serbestlik derecesi ve istenilen doğruluk oranına göre seçilen eşik değeri ile karşılaştırılır. Eşik değeri aşıldığı durumda sistemde arıza olduğu kabul edilir. Arıza tespit sisteminin ikinci aşamasında ise, hesaplanan normalize edilmiş inovasyon değeri kullanılarak hangi manyetometrenin arızalı çalıştığı tespit edilebilmektedir. Uygulanan algoritmanın çalışma prensibi gereğince, ölçüm sensöründe bir hata mevcudiyeti söz konusu olduğunda, genişletilmiş Kalman filtresi yerine gürbüz genişletilmiş Kalman filtresi devreye girmektedir. Aksi takdirde, genişletilmiş Kalman filtresi aynı şekilde çalışmaya devam etmektedir. Gürbüz genişletilmiş Kalman filtresi algoritmasında ek olarak hesaplanan ölçek faktörü, Kalman kazancını değiştirerek sensördeki hatanın elimine edilmesine olanak sağlamaktadır. Bu şekilde otonom olarak çalışan algoritma, yönelim açılarını ve açısal hızları başarılı bir şekilde tahmin edilebilmektedir. Simülasyon sonuçlarına göre, sisteme sürekli olarak arıza tanımlanması durumunda gürbüz genişletilmiş Kalman filtresinin biriken hatayı elimine etmede başarılı olmadığı görülmüştür. Bunun yerine, arıza yalnızca belirli bir iterasyon aralığında tanımlandığında gürbüz genişletilmiş Kalman filtresinin kabul edilebilir bir doğrulukla başarılı bir şekilde çalıştığı söylenebilir. Bu çalışmanın devamı olarak, sensörde meydana gelen hataların çeşitlerinin tespit edilmesi ve bu hataların giderilmesi için gereken kapsamlı senaryolar geliştirilebilir.

Yukarıda belirtilen tüm algoritmalar MATLAB programlama dili kullanılarak oluşturulmuş ve simülasyonlar bu ortamda gerçekleştirilmiştir. Simülasyonlar neticesinde elde edilen sonuçlarda Euler açılarının ve açısal hızların kestirimi, hata payları ve kovaryans analizleri ile birlikte sunulmuştur.

1. INTRODUCTION

One of the biggest problems in the space industry is that the payloads have a high amount of volume and mass. According to the Newton's second law, increasing in the mass wanted to put into space is directly increasing the required force. Therefore, the heaviest satellite means bigger rockets which provide more thrust. On the other hand, recent experiences showed that utilization of a satellite constellation is much more advantageous than one big satellite [1–5]. These advantageous can be explained such that production and testing of a satellite constellation would be much cheaper and easier. Also, a catastrophic failure can be lead to loss of the mission in case of a one big satellite; however, a constellation can be survived. As a consequence, a large interest has been aroused to develop micro systems such as pico-satellite for space technologies [6].

1.1 Literature Review

A pico-satellite is a class of small satellites, having an approximate volume of 1 liter and a mass under 1 kg [7]. When the satellites got smaller, all of the subsystems have to be miniaturized in order to fit into the available volume. This situation changes the description of the problem into another platform. For example in the case of the attitude determination, concessions have to be made for the accuracy of the sensors since traditional ones are heavy and large [8]. From a different perspective, pico-satellites generate minimal energy; therefore, passive methods with no energy consumption need to be used. Although some missions achieved on-board attitude determination, it is still not an easy task to accomplish [9, 10].

Attitude is the orientation of a defined spacecraft body coordinate system with respect to a defined external frame. Attitude determination is real-time or post-facto knowledge, within a given tolerance, of the spacecraft attitude. The attitude determination subsystem has to generate a specific moment in a specific direction for the sake of the mission. For managing attitude determination of a pico-satellite,

measurements from attitude sensors are used within various methods. Within a wide range of sensor types, sun sensors and magnetometers are the most preferred ones because of the fact that they are lightweight, reliable, and have low-power requirement [11]. Additionally, they can be run in a fully autonomous manner without a need for an external interference. Furthermore, they can be used in static and recursive attitude determination methods.

Static and recursive methods are the main methods used for the attitude determination purposes. They estimate the attitude angles by using information gathered from two or more vectors, for instance sun sensor and magnetometer measurements. Generally speaking, two or more vectors are determined analytically in the reference frame and compared with their measured counterparts in the body coordinate frame [12–16]. Beside analytical approaches, numerical methods are also very common for attitude determination and extensive review of these can be found in the studies by Hinks and Psiaki [17] and Markley and Mortari [18].

The coordinate systems used in attitude determination, body or inertial reference frames, can be transformed to each other using transformation matrices. The information gathered from sun sensors which indicate the unit vector towards the Sun and the Earth's magnetic field can be used to define reference directions [19]. Combination of the information gathered from these sensors, and sometimes rate gyro utilization, is typical in small satellites. Moreover, these information can be used as inputs for Kalman filters (KF) to estimate the attitude parameters of a satellite accurately.

Kalman filters have an outstanding reputation when it comes to the state estimation of the system and sensor kinetics and kinematics. As long as they are fed with priori mesaurements as mentioned earlier, they can predict the system states and calculate the residue. These facts made them perfect candidates for ground-based and on-board attitude determination systems. However, like most of the real world problems, the kinetics and kinematics of pico-satellites are inherently non-linear [20]. In order to tackle this nonlinearity and provide more reliable estimations, a newer version Kalman filter has been developed for the pico-satellite attitude estimation, called the extended Kalman filter (EKF) [21–25]. Normally KF is not applicable to nonlinear problems,

yet the use of Taylor Series expansion for linearization of the dynamic model tackles this issue and presents the EKF.

Implementation of EKFs can be achieved based on nonlinear or linear measurements. The first approach is the traditionally used EKF method while the latter is called as the nontraditional approach. In traditional EKF applications the measurement models are nonlinear because of the fact that inputs for the filter are chosen as nonlinear measurements. Contrary to this approach, nontraditional approach iteratively determines the attitude angles through vector measurement-based attitude determination methods. Subsequently, these angles become measurement inputs for the EKF, generating a linear measurement model [26–28].

Hajiyev and Bahar [29, 30] combined the algebraic method that uses a two-vector algorithm and EKF for attitude determination purposes, to determine the Euler angles and the angular velocities. Cordova-Alarcon et al. [31] used a modified version EKF for attitude estimation during the eclipse mode of a satellite. Considering the unavailability of the sun sensor during the eclipse phase, they used the Gauss-Newton method to accurately estimate the angular rates during the sun phase. Ke et al. [11] proposed a simplified EKF to address a near-Earth estimation problem of pico-satellites. The Jacobian calculations was simplified in order to reduce the filter's computation. The results proved the fast convergence and high accuracy characteristics of the proposed simplification.

However, EKF can not manage to keep up with the unexpected changes in the measurement system. These unexpected changes can be exemplified as malfunctions or unrealistic measurements which may lead to amplification of the background noise and suddenly changed filter outputs, resulting in filter crashing. An extensive overview of fault tolerant control systems was given by Jiang [32]. The fundamentals of fault tolerant control systems were explained including passive and active approaches and the historical developments were briefly described. In another study by Hwang et al. [33], different methods for fault detection, isolation and reconfiguration were examined, most important of which is innovation sequence.

Pirmoradi et al. proposed a new scheme for fault detection and diagnosis (FDD) for spacecraft attitude determination [34]. Utilization of rate gyros and vector sensors,

a unified attitude determination system was developed which is also capable of measuring the rate and angular position of the spacecraft. Evaluation of the measured data using a linearized Kalman filter which works with the system kinematics allows to obtain attitude estimation and the values of the gyro bias. This obtained information about attitude estimation and the values of the gyro bias is used to correct the faulty sensor measurements and avoid unbounded sensor measurements. The FDD algorithm combines the information from rotational dynamics and kinematics of a spacecraft with the measured data by sensor and implements model-based state estimation in order to predict the future sensor outputs. Lastly, EKFs are used to perform fault isolation in the system. Numerous statistical tests are performed to observe the innovation sequences of EKFs, detecting failures and localizing them in all AD sensors.

On the other hand, if the filter runs robustly, the situation and the risks can disappear [35–37]. Thus, the robust EKF (REKF) algorithm is presented and implemented to estimate the attitude parameters and its accuracy is tested. As required by the filter's working principle, the faulty measurements are used after scaling with small weights; thus, the correction of estimations can be isolated from them. This procedure is accomplished with help of a coefficient which is called as the measurement noise scale factor (MNSF). Jayaram developed a new fast converging extended Kalman filter for sensor fault detection and isolation [38]. The proposed filter uses innovative initialization of covariance matrix using system dynamics. The proposed nonlinear filter has been tested and compared with the classical Kalman filter schemes via simulations performed on the model of a space vehicle and has shown the benefits of the novel approach. The proposed method takes advantage of both the fast convergence capability and the robustness of numerical stability. Soken et al. studied the attitude estimation of pico-satellites in the presence of faulty measurements using REKF [39]. In this work, the faulty measurements were identified and corrected. Another study by Soken and Hajiyev two robust KFs were studied, namely, REKF and robust unscented Kalman filter (RUKF) and the results were compared [40]. Contrary to expectations, the robust Kalman filter is easy to implement to reduce the measurement noise and to estimate the attitude of pico-satellite.

1.2 Purpose of Thesis

Spacecraft navigation rely on attitude determination which requires the steps of data processing, computation and sometimes communication between the spacecraft and the ground stations. The obtained information is used to take relevant actions such as executing orbit maneuvers, engaging camera or deploying solar panels. However, if a delay within the computation process or a failure in the system occurs, it is inevitable to observe destructive results that may put the mission in danger.

Therefore, precautionary actions are required to solve the potential problems explained above. Despite the fact that the Extended Kalman Filter is a widely used method for attitude determination, they are inefficient while the spacecraft is spinning with considerable speed. To compensate this phase, less accurate yet fast responding attitude determination methods such as vector-based methods are examined. In that manner, in this thesis, static attitude determination methods are presented. First of them is named as two vector algorithm which is used to estimate the attitude angles. And, another method presented by Crassidis [41] is using least squares approach to compute the estimation of angular velocities. In addition, covariance analyses are carried out for both methods. Then, these vector-based methods are implemented in the Extended Kalman Filter algorithm to overcome the non-linear measurement issue. By doing so, the coarse attitude estimation acquired from vector-based methods are fed to the filter as measurement data to linearize the measurement model while increasing the accuracy. The resulting attitude estimations are compared with the estimations obtained by traditionally applied EKF.

Moreover, the failure in the attitude sensor is taken into consideration and methods to address this issue are investigated. These include early detection and isolation of faults. This leads to more autonomous pico-satellites with on-board detection and isolation systems to accomplish given missions even with the presence of faults in various components such as sensors and actuators. Subsequently, the EKF is enhanced to proceed in case of faulty measurements in the system and Robust Extended Kalman Filter is presented.

2. MATHEMATICAL MODELS

2.1 Pico-Satellite Dynamic Model

The derivation of the pico-satellite's kinematics equations by Euler angles allows to express the mathematical model with a six dimensional state vector. The vector becomes attitude Euler angle vector and the body angular rate vector with respect to the inertial axis frame. The attitude Euler angle vector consists of ϕ, θ, and ψ which are the roll angle about the x axis, the pitch angle about the y axis, and the yaw angle about the z axis, respectively. Hence,

$$\vec{x} = [\phi \quad \theta \quad \psi \quad \omega_x \quad \omega_y \quad \omega_z]^T \tag{2.1}$$

For consistency and clarity in further mathematical expressions, it is more convenient to express the body angular rate vector with respect to the inertial axis frame separately as $\vec{\omega}_{BI} = [\omega_x \quad \omega_y \quad \omega_z]^T$, where $\vec{\omega}_{BI}$ is the angular velocity vector of the body frame with respect to the inertial frame. Then, using the conservation of angular momentum, the dynamic equations of the satellite can be derived as follows [13]:

$$J\frac{d\vec{\omega}_{BI}}{dt} = \vec{N}_T - \vec{\omega}_{BI} \times (J\vec{\omega}_{BI}) \tag{2.2}$$

where $\mathbf{J}$ is the inertia matrix composed of principal moments of inertia as $\mathbf{J} = diag(J_x, J_y, J_z)$. $\vec{N}_T$ is the disturbance torque vector affecting the satellite as $\vec{N}_T = [N_{Tx}, N_{Ty}, N_{Tz}]^T$. Then, the pico-satellite's kinematic equations of motion in terms of Euler angles are given below:

$$\begin{bmatrix} \dot{\phi} \\ \dot{\theta} \\ \dot{\psi} \end{bmatrix} = \begin{bmatrix} cos(\psi) & -sin(\psi) & 0 \\ sin(\psi)/cos(\phi) & cos(\psi)/cos(\phi) & 0 \\ sin(\psi)tan(\phi) & cos(\psi)tan(\phi) & 1 \end{bmatrix} \begin{bmatrix} \omega_x \\ \omega_y \\ \omega_z \end{bmatrix} \tag{2.3}$$

2.2 Mathematical Models of Attitude Hardware

2.2.1 Magnetometer model

The pico-satellite considered in this work has a three axis magnetometer (TAM) being a sole measurement instrument. The mathematical measurement model of the magnetometer should be derived to implement Kalman filter algorithms.

During the satellite's navigation on its orbit, variations of the magnetic field will be apparent based on the orbital parameters, affecting the magnetic field vector. For the case in which those parameters are known, the magnetic field tensor vector affecting the satellite can be represented as a function of time analytically [27]. In the following equation, these terms are obtained in the orbit reference frame.

$$B_1(t_k) = \frac{M_e}{r_0^3}(cos(\omega_0 t_k)[cos(\varepsilon)sin(i) - sin(\varepsilon)cos(i)cos(\omega_e t_k)] - sin(\omega_0 t_k)sin(\varepsilon)sin(\omega_e t_k)) \tag{2.4}$$

$$B_2(t_k) = -\frac{M_e}{r_0^3}[cos(\varepsilon)cos(i) + sin(\varepsilon)sin(i)cos(\omega_e t_k)] \tag{2.5}$$

$$B_3(t_k) = \frac{2M_e}{r_0^3}(sin(\omega_0 t_k)[cos(\varepsilon)sin(i) - sin(\varepsilon)cos(i)cos(\omega_e t_k)] - 2cos(\omega_0 t_k)sin(\varepsilon)sin(\omega_e t_k)) \tag{2.6}$$

where the numerical values of the parameters can be listed as: the magnetic dipole moment of the Earth $M_e = 7.943 \times 10^{15}$ Wb.m, the Earth gravitational constant $\mu = 3.98601 \times 10^{14}$ m^3/s^2, the orbit inclination $i = 97^\circ$, the spin rate of the Earth $\omega_e = 7.29 \times 10^{-5}$ rad/s, the magnetic dipole tilt $\varepsilon = 11.7^\circ$, the orbital radius $r_0 = 6928140$ m. ω_0 denotes the angular velocity of the orbit with respect to the inertial frame, which can be found as $\omega_0 = (\mu / r_0^3)^{1/2}$.

The components of the magnetic field vector in the body frame are measured by the three magnetometers on-board. Therefore, in order to represent all the terms on the same axis frame, the magnetic field expressions have to turn into the orbital frame using direction cosine matrix **A**. The direction cosine matrix is given as:

$$\mathbf{A} = \begin{bmatrix} c(\psi)c(\theta) + s(\psi)s(\theta)s(\phi) & s(\psi)c(\phi) & -c(\psi)s(\theta) + s(\psi)c(\theta)s(\phi) \\ -s(\psi)c(\theta) + c(\psi)s(\theta)s(\phi) & c(\psi)c(\phi) & s(\psi)s(\theta) + c(\psi)c(\theta)s(\phi) \\ c(\phi)s(\theta) & -s(\phi) & c(\phi)c(\theta) \end{bmatrix} \tag{2.7}$$

In A matrix, cosine and sine functions are denoted as $c(.)$ and $s(.)$. Following the transformation, the overall measurement model can represented as follows:

$$\begin{bmatrix} B_x(\phi,\theta,\psi,t_k) \\ B_y(\phi,\theta,\psi,t_k) \\ B_z(\phi,\theta,\psi,t_k) \end{bmatrix} = \mathbf{A} \begin{bmatrix} B_1(t_k) \\ B_2(t_k) \\ B_3(t_k) \end{bmatrix} + n_1 \tag{2.8}$$

where $B_1(t_k), B_2(t_k)$ and $B_3(t_k)$ are the components of the Earth's magnetic field vector in the orbit frame as a function of time. Then, the measured magnetic field vector components of the Earth in the body frame as a function of time and Euler angles are given by $B_x(\phi,\theta,\psi,t_k), B_y(\phi,\theta,\psi,t_k)$ and $B_z(\phi,\theta,\psi,t_k)$. Additionally, n_1 is the zero mean Gaussian white noise with the characteristic of

$$E[n_{1k}n_{1j}^T] = I_{3\times3}\sigma_m^2\delta_{kj} \tag{2.9}$$

where $I_{3\times3}$, σ_m, and δ_{kj} denote three-dimensional identity matrix, standard deviation of each magnetometer error, and the Kronecker symbol, respectively.

2.2.2 Sun sensor model

The sun model is also integrated to the mathematical model, which determines the position of the Sun in the inertial reference system, in order to constantly check if the Sun is blocked by the Earth or not. As the spacecraft orbits the Earth also revolves around the Sun, its inertial sun vector varies constantly during the motion of the satellite through its orbit.When it comes to satellites which has much more smaller orbital radius than astronomical unit such as LEO satellites, the cyclic changes are much lower than both sun sensors correctness level and sufficient precision of the reference model.Therefore, a simplification is suggested which assumes the Sun line is independent of the spacecraft position and always parallel to the vector from the Earth to the Sun. This assumption leads to the following:

$$\hat{s}_{ECI} \approx \hat{s}_{ECI}^{Earth\rightarrow Sun} \tag{2.10}$$

The real motion of the Earth around the Sun that is inertially fixed can be expressed as the Sun orbiting the Earth which has a fixed position in the inertial space [42]. The governing equation of this model is given in equation 2.11. By definition, the right

ascension of the ascending node of this hypothesized orbit of the Sun around the Earth is 0°. The reference epoch of this first-order model is the 1st of January 2000, 12:00:00 pm, or 2451545.0 Julian Date (JD).

$$T = \frac{JD - 2451545.0}{36525} \tag{2.11}$$

where

$$\begin{aligned} JD = 367y - INT\left\{\frac{7\{y+INT[(m+9)/12]\}}{4}\right\} + INT\left\{\frac{275m}{9}\right\} \\ + \frac{h+min/60+s/3600}{24} + d + 1721013.5 \end{aligned} \tag{2.12}$$

in days. The mean longitude of the sun is given as follows:

$$\lambda_{M_{Sun}} = 280.460^\circ + 36000.770T \tag{2.13}$$

The mean anomaly of the sun is

$$M_{Sun} = 357.5277233^\circ + 35999.05034T \tag{2.14}$$

The ecliptic longitude of the sun introduces the correction of the Sun "traveling" on an eccentric orbit.

$$\lambda_{ecliptic} = \lambda_{M_{Sun}} + 1.914666471^\circ \sin(M_{Sun}) + 0.019994643^\circ \sin(2M_{Sun}) \tag{2.15}$$

The linear model of the ecliptic of the Sun is

$$\varepsilon = 23.439291^\circ - 0.0130042T \tag{2.16}$$

which is an almost constant value. Finally the unit sun vector in the inertial frame can be expressed as follows:

$$\hat{s}_{ECI} = \begin{bmatrix} \cos\lambda_{ecliptic} \\ \sin\lambda_{ecliptic}\cos\varepsilon \\ \sin\lambda_{ecliptic}\sin\varepsilon \end{bmatrix} \tag{2.17}$$

In order to represent the sun vector in the orbit coordinates, the transformation matrix from ECI to the orbit frame T_{ECI}^{Orbit} has to be determined. Here u can be propagated through the orbit with $\Delta u = 2\pi\frac{\Delta t}{T}[rad]$.

$$\mathbf{T}_{ECI}^{Orbit} = \begin{bmatrix} c(u)c(i)c(\lambda) - s(u)s(\lambda) & c(u)s(i) & -c(u)c(i)s(\lambda) - s(u)c(\lambda) \\ -s(i)c(\lambda) & c(i) & s(i)s(\lambda) \\ s(u)s(i)c(\lambda) - c(u)s(\lambda) & s(u)s(i) & -s(u)c(i)s(\lambda) - c(u)c(\lambda) \end{bmatrix} \tag{2.18}$$

In $\mathbf{T}_{ECI}^{Orbit}$ matrix, cosine and sine functions are denoted as $c(.)$ and $s(.)$. Eventually, the sun vector in the orbit frame can be written as follows:

$$\mathbf{s}_O = T_{ECI}^{Orbit} \times \hat{s}_{ECI} \tag{2.19}$$

The vectors coming from the sensors in body frame can be modeled as:

$$\begin{bmatrix} s_{B_x} \\ s_{B_y} \\ s_{B_z} \end{bmatrix} = A \begin{bmatrix} s_{O_x} \\ s_{O_y} \\ s_{O_z} \end{bmatrix} + \eta \tag{2.20}$$

Here, $\begin{bmatrix} s_{B_x} & s_{B_y} & s_{B_z} \end{bmatrix}^T$ is a representation of the measured sun direction vector in body coordinates and $\begin{bmatrix} s_{O_x} & s_{O_y} & s_{O_z} \end{bmatrix}^T$ in orbit coordinates. η is the zero mean Gaussian white noise with the characteristic of:

$$E\left[\eta_k \eta_j^T\right] = I_{3\times 3}\sigma_m^2 \delta_{kj} \tag{2.21}$$

Here σ_m is the standard deviation of each sun sensor error and δ_{kj} is the Kronecker symbol.

3. STATIC ATTITUDE DETERMINATION

3.1 Attitude Estimation with Algebraic Method

The algebraic method utilizes vectors to determine the transformation matrix. Two vectors, u and v, are observed to form the transformation matrix or attitude matrix (A). u and v are any vectors defining an orthogonal coordinate system. The equations associated with the static attitude determination can be defined based on two vector algorithm method.

3.1.1 Two vector algorithm

$$\hat{n} = \hat{u} \times \hat{v} \tag{3.1}$$

The reference matrix M_R can be calculated using the two reference vectors in orbital coordinates, $\hat{u}_R$ and $\hat{v}_R$.

$$M_R = \begin{bmatrix} \hat{u}_R & \vdots & \hat{v}_R & \vdots & \hat{n}_R \end{bmatrix} \tag{3.2}$$

Similarly, the two measured vectors in the spacecraft body coordinates, $\hat{u}_B$ and $\hat{v}_B$, the body matrix can be obtained as

$$M_B = \begin{bmatrix} \hat{u}_B & \vdots & \hat{v}_B & \vdots & \hat{n}_B \end{bmatrix} \tag{3.3}$$

The attitude matrix then can be obtained similar to Equation 3.10, as follows:

$$M_B = AM_R, \quad A = M_B M_R^{-1} \tag{3.4}$$

In this study, u and v are selected as the sun direction (S) and the magnetic field vector (H). The two vector algorithm is simulated and the results are given in Figures 3.1, 3.2, and 3.3. The upper graphs show that the comparison between actual attitude

angles computed from satellite dynamics and the attitude angles estimated by two vector algorithm. As well as, the bottom graphs show that the error value between them.

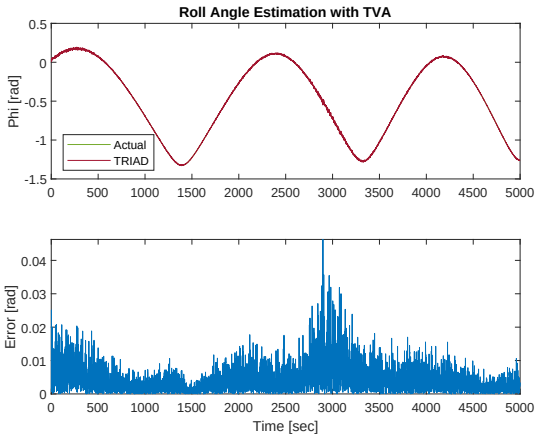

Figure 3.1 : Roll angle estimation values.

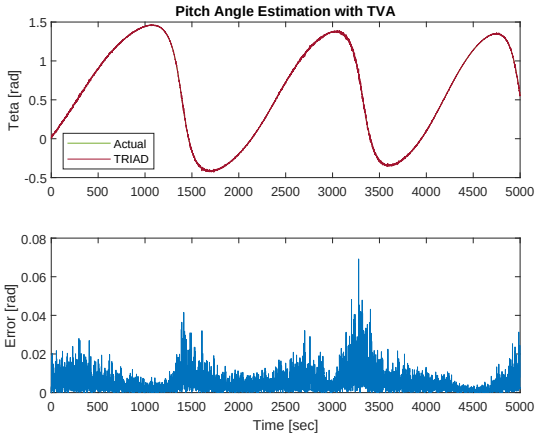

Figure 3.2 : Pitch angle estimation values.

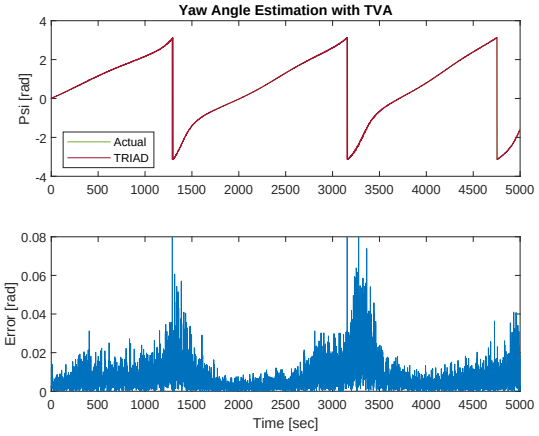

Figure 3.3 : Yaw angle estimation values.

As it can be seen in the figures, the estimated attitude angle values pursue similar trend to the actual attitude angles. Additionally, the error values are increased as the pitch angle closes to 90° which is an expected phenomena.

3.1.1.1 Two vector algorithm with normalized vectors

The proposed two vector algorithm can also be implemented by using an orthogonal set of $\hat{u}$ and $\hat{v}$ vectors. This way is also known as three axial attitude determination (TRIAD).

$$\hat{q} = \hat{u} \tag{3.5}$$

$$\hat{r} = \frac{\hat{u} \times \hat{v}}{|\hat{u} \times \hat{v}|} \tag{3.6}$$

$$\hat{s} = \hat{q} \times \hat{r} \tag{3.7}$$

Aforementioned two reference vectors in orbital coordinates $\hat{u}_R$ and $\hat{v}_R$ can be used to calculate the reference matrix M_R as follows:

$$M_R = \begin{bmatrix} \hat{q}_R & \vdots & \hat{r}_R & \vdots & \hat{s}_R \end{bmatrix} \tag{3.8}$$

Using $\hat{u}_B$ and $\hat{v}_B$, the measured vectors in the spacecraft body coordinates, the body matrix M_B can be obtained as follows:

$$M_B = \begin{bmatrix} \hat{q}_B & \vdots & \hat{r}_B & \vdots & \hat{s}_B \end{bmatrix} \tag{3.9}$$

Finally, the attitude matrix is calculated as

$$M_B = AM_R, \quad A = M_B M_R^{-1} \tag{3.10}$$

TRIAD algorithm is simulated with the same conditions as two vector algorithm and the results are given in Figures 3.4, 3.5, and 3.6.

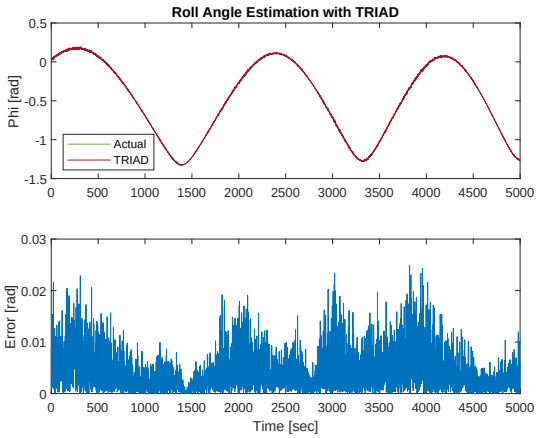

Figure 3.4 : Roll angle estimation values.

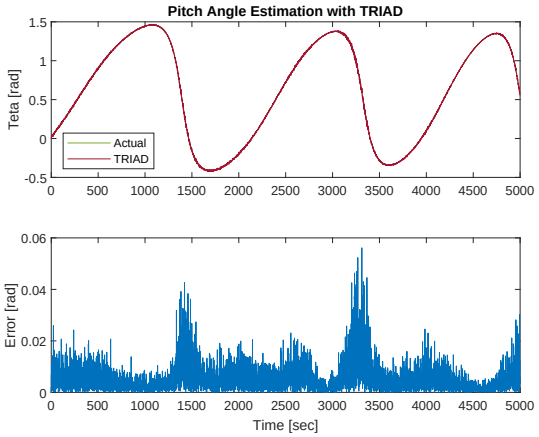

Figure 3.5 : Pitch angle estimation values.

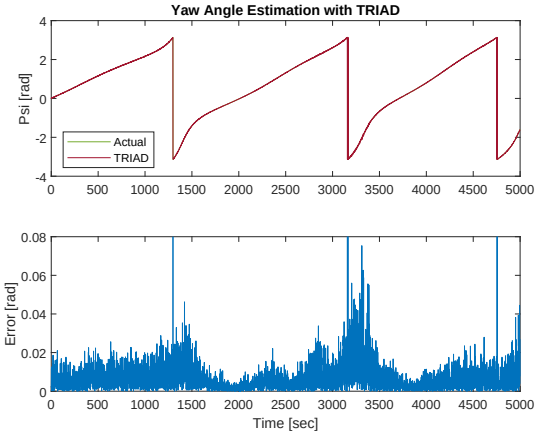

Figure 3.6 : Yaw angle estimation values.

The results are similar with two vector algorithm. Since the obtained error values are changing through different time steps, there can not be a sharp judgment such as one of the algorithm is better.

3.1.2 Covariance analysis

In order to calculate the attitude covariance matrix [43] in the Euler form, the Cartesian attitude covariance matrix ($P_{\theta\theta}$) must be calculated initially.

$$P_{\theta\theta} = \sigma_1^2 I + \frac{1}{|\vec{u}_B \times \vec{v}_B|^2}\left[\left(\sigma_2^2 - \sigma_1^2\right)\vec{u}_B\vec{u}_B^T + \sigma_1^2\left(\vec{u}_B.\vec{v}_B\right)\left(\vec{u}_B\vec{v}_B^T + \vec{v}_B\vec{u}_B^T\right)\right] \tag{3.11}$$

where σ_1^2 and σ_2^2 are the variance of the magnetometer and the variance of sun sensor, respectively, while I is 3x3 unit matrix.

The simulated two vector algorithm presents the variance of estimation error which can be seen in Figure 3.7. The graphs are shown that roll, pitch, and yaw angle variances of estimation errors respectively.

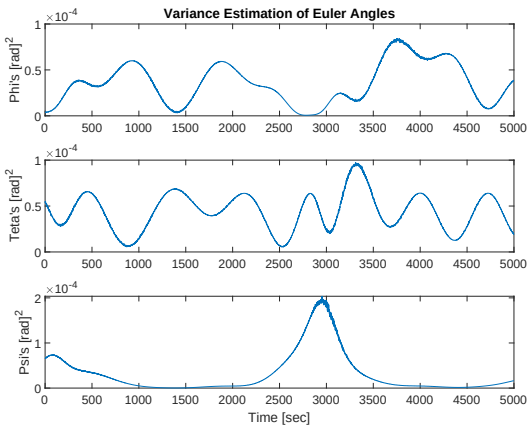

Figure 3.7 : Variance of estimation error.

As a result of that, the variance values of Euler angle estimation errors are found to be within acceptable level.

3.2 Attitude Rate Estimation Algorithm

The angular velocities are determined by a least-square approach that uses the information obtained solely from sensor body measurements. For conciseness, this

approach will be referred to as ARES in this study. Now look at given unit vector of measurement model below:

$$\tilde{b}_i(t_k) = A(t_k)r_i + v_i(t_k) \tag{3.12}$$

where $b_i(t_k)$ is the i^{th} body measurement vector, $A(t_k)$ is the orthogonal attitude matrix, r_i is the measurement vector, and $v_i(t_k)$ is the measurement noise which is given by a zero-mean Gaussian white-noise process.

The goal of this method is to determine an angular velocity estimate with no dependence on attitude and reference vectors. The detailed derivation of the corresponding equations is extensively given in by Crassidis [41] and skipped here for conciseness. The equation for a linear least-square analysis using all measurement vectors is given as follows:

$$\hat{\omega}(t_k) = \frac{1}{\Delta t}\left\{\sum_{i=1}^{n} \bar{\sigma}_i^{-2}\left[\tilde{b}_i(t_k)\times\right]^T\left[\tilde{b}_i(t_k)\times\right]\right\}^{-1}\sum_{i=1}^{n} \bar{\sigma}_i^{-2}\left[\tilde{b}_i(t_k)\times\right]^T\tilde{b}_i(t_{k+1}) \tag{3.13}$$

where $[b(t_k)\times]$ is the cross-product matrix, given as

$$[b(t_k)\times] = \begin{bmatrix} 0 & -b_3(t_k) & b_2(t_k) \\ b_3(t_k) & 0 & -b_1(t_k) \\ -b_2(t_k) & b_1(t_k) & 0 \end{bmatrix} \tag{3.14}$$

where $\hat{\omega}(t_k)$ is the estimation of $\omega(t_k)$, and $\bar{\sigma}_i^2 \equiv 2\sigma_i^2/\Delta t^2$ is the effective measurement error variance. The only required parameters to achieve an angular velocity estimate are the body vector measurements, sampling interval, and measurement covariance.

In this study, the measurement models are selected as the sun sensor and the magnetometer. The ARES algorithm is simulated and the results are given in Figures 3.8, 3.9, and 3.10. The upper graphs show that the comparison between actual attitude angle rates computed from satellite dynamics and the attitude angle rates estimated by ARES algorithm. As well as, the bottom graphs show that the error value between them.

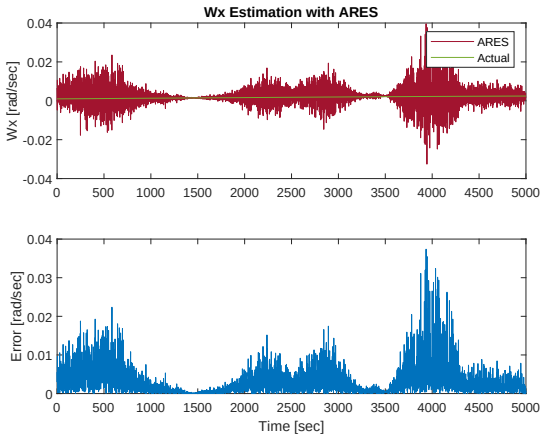

Figure 3.8 : W_x estimation values.

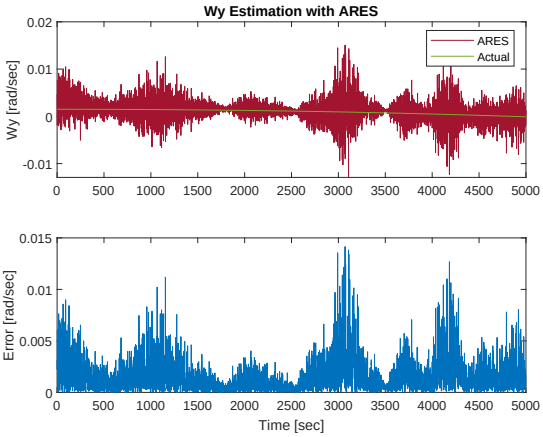

Figure 3.9 : W_y estimation values.

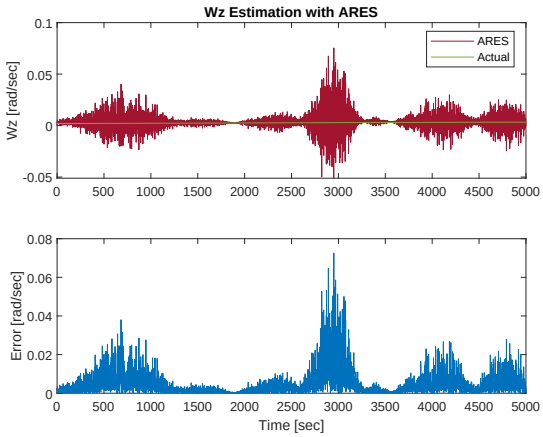

Figure 3.10 : W_z estimation values.

As can be seen in the figures above, the result of the ARES algorithm are not quite successful. The reason of that is in the original method, there are used only star sensor

measurements with a changing number of star vectors for calculation. Since the star sensor are more accurate than the sun sensor and the magnetometer, the estimated angular velocity values could not catch the real data.

3.2.1 Covariance analysis

The derivation of the estimate error covariance can be found in [41]. The predicted error covariance is simply given by

$$P_{t_k} = \left\{ \sum_{i=1}^{n} \bar{\sigma}_i^{-2} \left[\tilde{b}_i(t_k) \times \right]^T \left[\tilde{b}_i(t_k) \times \right] \right\}^{-1} \tag{3.15}$$

The simulated ARES algorithm presents the variance of estimation error which can be seen in Figure 5.1. The graphs are shown that roll, pitch, and yaw angle rate variances of estimation errors respectively.

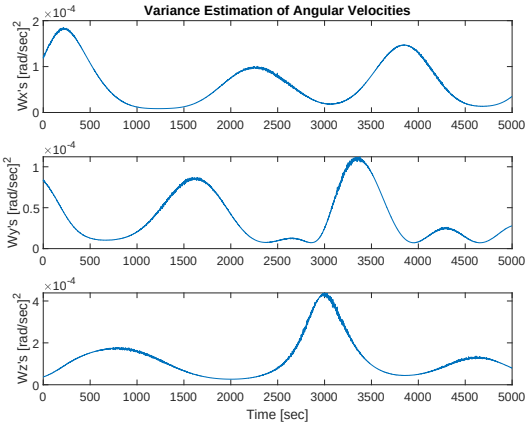

Figure 3.11 : Variance of estimation error.

When the variance graphs are investigated, it is seen that the error values are increasing at the covariance graph pick points. Therefore, it can be said that the overall algorithm is implemented successfully.

4. RECURSIVE ATTITUDE DETERMINATION

4.1 Extended Kalman Filter Algorithm

For the application of Extended Kalman filter algorithm to pico satellites, consider the following case of nonlinear systems including white noise in it where noisy measurements are given as follows [44]:

$$x(t_{k+1}) = \phi[x(t_k), t_k] + \omega(t_k) \tag{4.1}$$

$$z(t_k) = h[x(t_k), t_k] + v(t_k) \tag{4.2}$$

where $x(t_{k+1})$, $z(t_k)$, and $w(t_k)$ denote the state vector at time t_{k+1}, the measurement and the system noise at time t_k, respectively. Additionally, $v(t_k)$, $\phi[x(t_k), t_k]$, and $h[x(t_k), t_k]$ are the measurement noise, the non-linear state transition function which draws the route from the present state to the further state, and a non-linear measurement model which draws the route from the present state to the measurements at time t_k, respectively.

The two noise vectors, $v(t_k)$ and $w(t_k)$ are assumed to be linearly additive Gaussian and temporally uncorrelated with zero mean. This assumption can formulated as follows:

$$E[\omega(t_k)] = E[v(t_k)] = 0, \quad \forall t_k \tag{4.3}$$

with the following covariances:

$$E[\omega(i)\omega^T(j)] = Q(i)\delta_{ij} \tag{4.4}$$

$$E[v(i)v^T(j)] = R(i)\delta_{ij} \tag{4.5}$$

where δ_{ij} is the Kronecker symbol. Additionally, it is typically assumed that the process and measurement noises are not correlated.

$$E[\omega(i)v^T(j)] = 0, \quad \forall i, j. \tag{4.6}$$

In this study, a real-time linear Taylor approximation is considered for the system function which estimate previous state and the observation function which gives predicted position. The resulting Kalman filter is named as the Extended Kalman Filter (EKF), algorithm of which can be defined with the following equations [45]:

The estimation expression can be written as

$$\hat{x}(t_{k+1}) = \hat{x}(t_{k+1}, t_k) + K(t_{k+1}) \times \{z(t_{k+1}) - h[\hat{x}(t_{k+1}/t_k), t_{k+1}]\}. \tag{4.7}$$

The extrapolation equation is obtained as

$$\hat{x}(t_{k+1}/t_k) = \phi[\hat{x}(t_k), t_k]. \tag{4.8}$$

Then, the filter gain of the EKF is given as

$$K(t_{k+1}) = P(t_{k+1}/t_k)H^T(t_{k+1}) \times [H(t_{k+1})P(t_{k+1}/t_k)H^T(t_{k+1}) + R(t_k)]^{-1} \tag{4.9}$$

where $H(t_{k+1}) = \dfrac{\partial h[\hat{x}(t_{k+1}/t_k), t_{k+1}]}{\partial \hat{x}(t_{k+1}/t_k)}$ is the measurement matrix, expressed in terms of partial derivatives.

The covariance matrix of the extrapolation error is given as

$$P(t_{k+1}/t_k) = \frac{\partial \phi[\hat{x}(t_k), t_k]}{\partial \hat{x}(t_k)} P(t_k/t_k) \times \frac{\partial \phi^T[\hat{x}(t_k), t_k]}{\partial \hat{x}(t_k)} + Q(t_k) \tag{4.10}$$

The covariance matrix of the filtering error is written as

$$P(t_{k+1}/t_{k+1}) = [I - K(t_{k+1})H(t_{k+1})]P(t_{k+1}/t_k). \tag{4.11}$$

The filter, equations of which are given above in Equations 4.7-4.11, is called the EKF.

4.2 Measurement Models

In this study, different EKF approaches are designed by changing the observation model while using the same EKF schema. First of all, in the classical approach, the observation model is constructed with magnetometer and sun sensor measurements as given in Section 2.2. As described in the Section 4.1, the measurement vector and the measurement matrix can be written as,

$$\mathbf{z}(t_k) = \begin{bmatrix} B_x(t_k) & B_y(t_k) & B_z(t_k) & s_{B_x}(t_k) & s_{B_y}(t_k) & s_{B_z}(t_k) \end{bmatrix} \tag{4.12}$$

$$\mathbf{H} = \begin{bmatrix} \frac{\partial(H_{B_1})}{\partial\phi} & \frac{\partial(H_{B_1})}{\partial\theta} & \frac{\partial(H_{B_1})}{\partial\psi} & \frac{\partial(H_{B_1})}{\partial\omega_x} & \frac{\partial(H_{B_1})}{\partial\omega_y} & \frac{\partial(H_{B_1})}{\partial\omega_z} \\ \frac{\partial(H_{B_2})}{\partial\phi} & \frac{\partial(H_{B_2})}{\partial\theta} & \frac{\partial(H_{B_2})}{\partial\psi} & \frac{\partial(H_{B_2})}{\partial\omega_x} & \frac{\partial(H_{B_2})}{\partial\omega_y} & \frac{\partial(H_{B_2})}{\partial\omega_z} \\ \frac{\partial(H_{B_3})}{\partial\phi} & \frac{\partial(H_{B_3})}{\partial\theta} & \frac{\partial(H_{B_3})}{\partial\psi} & \frac{\partial(H_{B_3})}{\partial\omega_x} & \frac{\partial(H_{B_3})}{\partial\omega_y} & \frac{\partial(H_{B_3})}{\partial\omega_z} \\ \frac{\partial(H_{s_1})}{\partial\phi} & \frac{\partial(H_{s_1})}{\partial\theta} & \frac{\partial(H_{s_1})}{\partial\psi} & \frac{\partial(H_{s_1})}{\partial\omega_x} & \frac{\partial(H_{s_1})}{\partial\omega_y} & \frac{\partial(H_{s_1})}{\partial\omega_z} \\ \frac{\partial(H_{s_2})}{\partial\phi} & \frac{\partial(H_{s_2})}{\partial\theta} & \frac{\partial(H_{s_2})}{\partial\psi} & \frac{\partial(H_{s_2})}{\partial\omega_x} & \frac{\partial(H_{s_2})}{\partial\omega_y} & \frac{\partial(H_{s_2})}{\partial\omega_z} \\ \frac{\partial(H_{s_3})}{\partial\phi} & \frac{\partial(H_{s_3})}{\partial\theta} & \frac{\partial(H_{s_3})}{\partial\psi} & \frac{\partial(H_{s_3})}{\partial\omega_x} & \frac{\partial(H_{s_3})}{\partial\omega_y} & \frac{\partial(H_{s_3})}{\partial\omega_z} \end{bmatrix} \tag{4.13}$$

where $AxB = \begin{bmatrix} H_{B_1} & H_{B_2} & H_{B_3} \end{bmatrix}^T$ and $Axs = \begin{bmatrix} H_{s_1} & H_{s_2} & H_{s_3} \end{bmatrix}^T$.

Also, the covariance of the measurement matrix, $\mathbf{R}$, can be generated as a square matrix which diagonal elements are the variances of magnetometer and sun sensor measurement noises. For the second approach, linear Euler angle measurements which is the result of TRIAD (Section 3.1.1.1) are taken as observation model. In this case, the measurement vector and the measurement matrix are given below,

$$\mathbf{z}(t_k) = \begin{bmatrix} \phi_{TRIAD}(t_k) & \theta_{TRIAD}(t_k) & \psi_{TRIAD}(t_k) \end{bmatrix} \tag{4.14}$$

$$\mathbf{H} = \begin{bmatrix} 1 & 0 & 0 & 0 & 0 & 0 \\ 0 & 1 & 0 & 0 & 0 & 0 \\ 0 & 0 & 1 & 0 & 0 & 0 \end{bmatrix} \tag{4.15}$$

Additionally, the covariance of the measurement matrix, **R**, can be generated as a square matrix which diagonal elements are the variances of attitude measurement noises found by TRIAD algorithm. The presented approach is called non-traditional EKF, the structural scheme of non-traditional EKF can be seen in Figure 4.1.

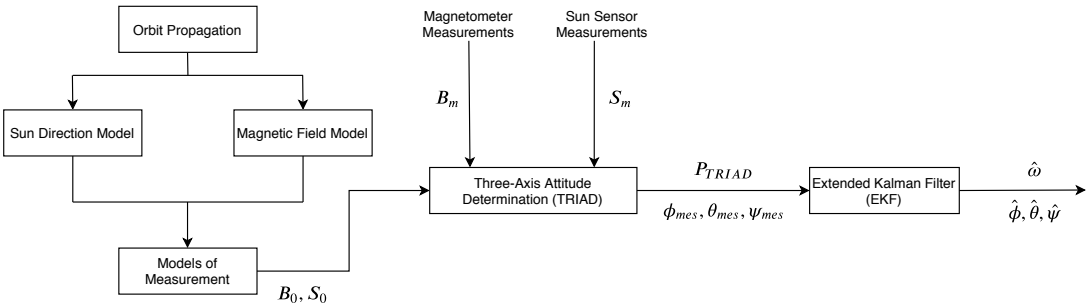

Figure 4.1 : Structural scheme of non-traditional EKF with TRIAD estimation.

Further, this approach can be improved by extending the measurement vector with addition of angle rate measurements found by ARES (Section 3.2). With this extension, the measurement vector and the measurement matrix are became,

$$\mathbf{z}(t_k) = \begin{bmatrix} \phi_{TRIAD}(t_k) & \theta_{TRIAD}(t_k) & \psi_{TRIAD}(t_k) & \omega_{x_{ARES}}(t_k) & \omega_{y_{ARES}}(t_k) & \omega_{z_{ARES}}(t_k) \end{bmatrix} \quad (4.16)$$

$$\mathbf{H} = \begin{bmatrix} 1 & 0 & 0 & 0 & 0 & 0 \\ 0 & 1 & 0 & 0 & 0 & 0 \\ 0 & 0 & 1 & 0 & 0 & 0 \\ 0 & 0 & 0 & 1 & 0 & 0 \\ 0 & 0 & 0 & 0 & 1 & 0 \\ 0 & 0 & 0 & 0 & 0 & 1 \end{bmatrix} \quad (4.17)$$

The covariance of the measurement matrix, **R**, is generated with the variances of attitude and attitude rate measurement noises as well which found by TRIAD and ARES algorithm respectively. The structural scheme of stated approach is given in Figure 4.2.

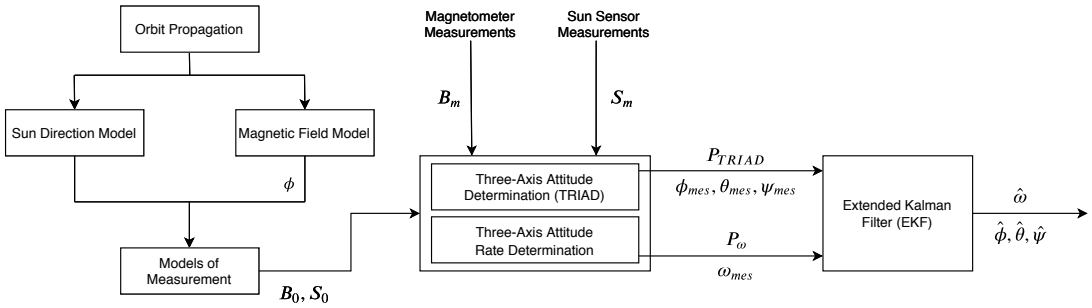

Figure 4.2 : Structural scheme of non-traditional EKF with TRIAD and ARES estimations.

The traditional EKF algorithm that described in the first place is taken only angle estimations as observation model. By getting inspiration from the non-traditional EKF, one more approach is presented. In this last approach, the measurement vector is constructed additionally with the attitude rate estimations found by ARES. For this case, the measurement vector and the measurement matrix can be written as,

$$\mathbf{z}(t_k) = \begin{bmatrix} B_x(t_k) & B_y(t_k) & B_z(t_k) & s_{B_x}(t_k) & s_{B_y}(t_k) & s_{B_z}(t_k) & \omega_{x_{ARES}}(t_k) & \omega_{y_{ARES}}(t_k) & \omega_{z_{ARES}}(t_k) \end{bmatrix} \tag{4.18}$$

$$\mathbf{H} = \begin{bmatrix} \frac{\partial(H_{B_1})}{\partial\phi} & \frac{\partial(H_{B_1})}{\partial\theta} & \frac{\partial(H_{B_1})}{\partial\psi} & \frac{\partial(H_{B_1})}{\partial\omega_x} & \frac{\partial(H_{B_1})}{\partial\omega_y} & \frac{\partial(H_{B_1})}{\partial\omega_z} & 0 & 0 & 0 \\ \frac{\partial(H_{B_2})}{\partial\phi} & \frac{\partial(H_{B_2})}{\partial\theta} & \frac{\partial(H_{B_2})}{\partial\psi} & \frac{\partial(H_{B_2})}{\partial\omega_x} & \frac{\partial(H_{B_2})}{\partial\omega_y} & \frac{\partial(H_{B_2})}{\partial\omega_z} & 0 & 0 & 0 \\ \frac{\partial(H_{B_3})}{\partial\phi} & \frac{\partial(H_{B_3})}{\partial\theta} & \frac{\partial(H_{B_3})}{\partial\psi} & \frac{\partial(H_{B_3})}{\partial\omega_x} & \frac{\partial(H_{B_3})}{\partial\omega_y} & \frac{\partial(H_{B_3})}{\partial\omega_z} & 0 & 0 & 0 \\ \frac{\partial(H_{s_1})}{\partial\phi} & \frac{\partial(H_{s_1})}{\partial\theta} & \frac{\partial(H_{s_1})}{\partial\psi} & \frac{\partial(H_{s_1})}{\partial\omega_x} & \frac{\partial(H_{s_1})}{\partial\omega_y} & \frac{\partial(H_{s_1})}{\partial\omega_z} & 0 & 0 & 0 \\ \frac{\partial(H_{s_2})}{\partial\phi} & \frac{\partial(H_{s_2})}{\partial\theta} & \frac{\partial(H_{s_2})}{\partial\psi} & \frac{\partial(H_{s_2})}{\partial\omega_x} & \frac{\partial(H_{s_2})}{\partial\omega_y} & \frac{\partial(H_{s_2})}{\partial\omega_z} & 0 & 0 & 0 \\ \frac{\partial(H_{s_3})}{\partial\phi} & \frac{\partial(H_{s_3})}{\partial\theta} & \frac{\partial(H_{s_3})}{\partial\psi} & \frac{\partial(H_{s_3})}{\partial\omega_x} & \frac{\partial(H_{s_3})}{\partial\omega_y} & \frac{\partial(H_{s_3})}{\partial\omega_z} & 0 & 0 & 0 \\ 0 & 0 & 0 & 0 & 0 & 0 & 1 & 0 & 0 \\ 0 & 0 & 0 & 0 & 0 & 0 & 0 & 1 & 0 \\ 0 & 0 & 0 & 0 & 0 & 0 & 0 & 0 & 1 \end{bmatrix} \tag{4.19}$$

where $AxB = \begin{bmatrix} H_{B_1} & H_{B_2} & H_{B_3} \end{bmatrix}^T$ and $Axs = \begin{bmatrix} H_{s_1} & H_{s_2} & H_{s_3} \end{bmatrix}^T$.

The covariance of the measurement matrix, **R**, can be generated as a square matrix which diagonal elements are the variances of magnetometer and sun sensor measurement noises, and the variances of attitude rate measurement noises found by ARES algorithm respectively.

5. SIMULATIONS

Simulations are executed for 5000 seconds with a sampling time of $\Delta t = 1$ second. The inertia matrix of the pico satellite model used in the simulations is given as

$$J = \begin{bmatrix} 2.1 \times 10^{-3} & 0 & 0 \\ 0 & 2.0 \times 10^{-3} & 0 \\ 0 & 0 & 1.9 \times 10^{-3} \end{bmatrix} kg.m^2 \tag{5.1}$$

In addition, the satellite's operational orbit is identified as circular orbit at an altitude of r = 550 km. The additional orbit information needed for the magnetometer and sun sensor models are taken as stated in the Section 2.2.1 and 2.2.2.

Measurement values which constitute sensor modelling are determined as zero mean Gaussian white noise. Besides, the standard deviation is taken as $\sigma_m = 0.008\ \mu T$ and $\sigma_s = 0.002$ for the magnetometer and the sun sensor respectively.

The simulations are realized with given conditions and the results are shown in the corresponding subsections. The figures consist of three subplots in which the upper graphs exhibit the actual and the estimated state vector components computed from satellite dynamics and the selected Kalman filtering approach, respectively. Additionally, the middle graphs indicate the error value between them while the lower graphs representing the variance of estimation errors.

5.1 Traditional EKF Estimations

The results obtained by using traditional EKF are given in Figures 5.1, 5.2, 5.3, 5.4, 5.5, and 5.6.

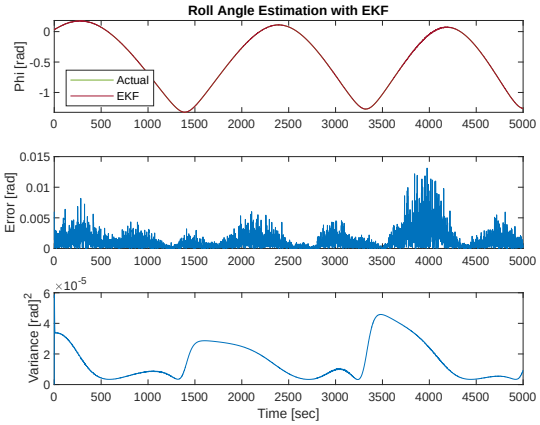

Figure 5.1 : Roll angle estimation values with traditional EKF.

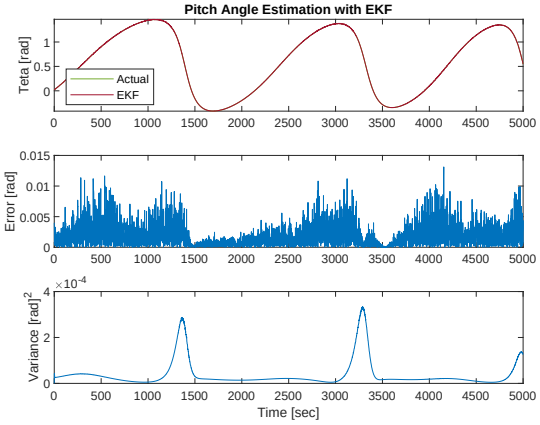

Figure 5.2 : Pitch angle estimation values with traditional EKF.

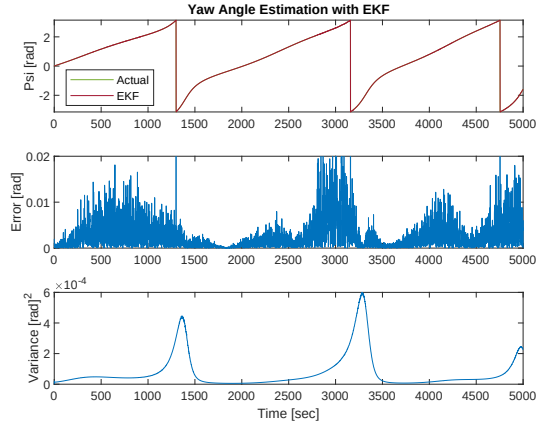

Figure 5.3 : Yaw angle estimation values with traditional EKF.

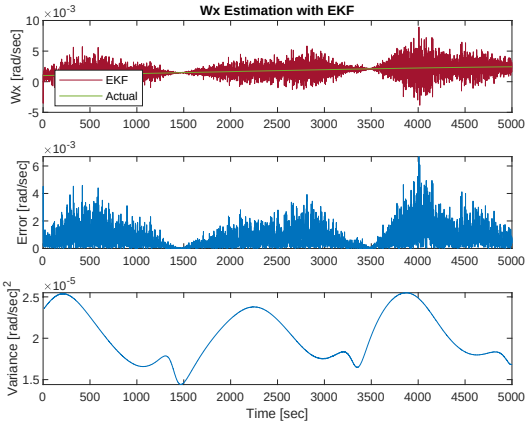

Figure 5.4 : ω_x estimation values with traditional EKF.

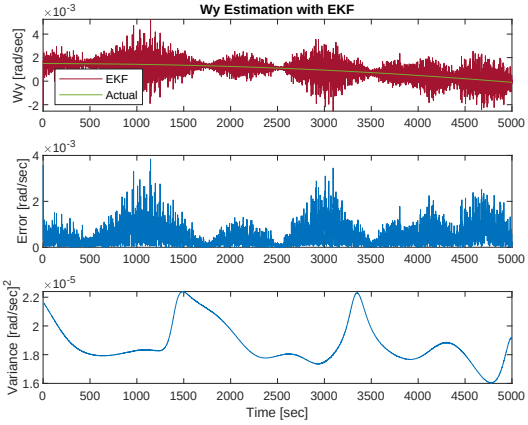

Figure 5.5 : ω_y estimation values with traditional EKF.

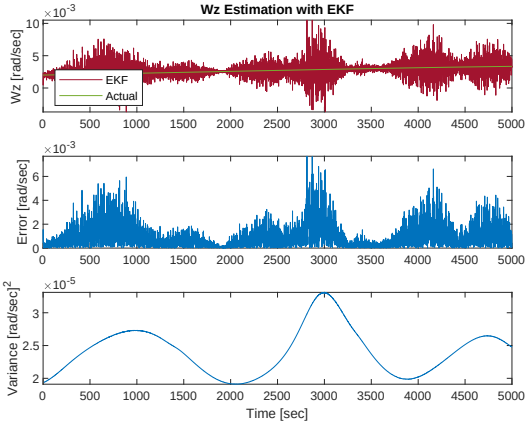

Figure 5.6 : ω_z estimation values with traditional EKF.

As it can be seen in the figures, the estimated state vector components pursue similar trend to the actual ones. Additionally, the error values are increased as the pitch angle

closes to 90° which is an expected phenomena. Also, the variance values of state vector estimation errors are found to be within acceptable level.

5.2 Non-Traditional EKF Estimations with TRIAD Measurement

The estimation results obtained by using non-traditional EKF with TRIAD measurements are given in Figures 5.7, 5.8, 5.9, 5.10, 5.11, and 5.12.

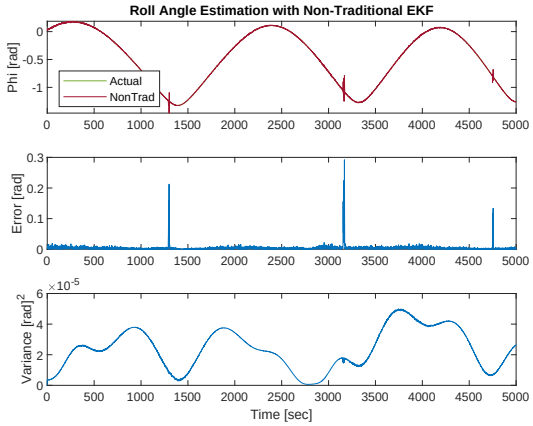

Figure 5.7 : Roll angle estimation values with non-traditional EKF.

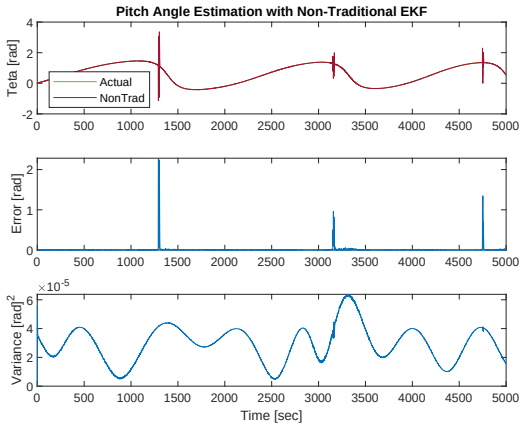

Figure 5.8 : Pitch angle estimation values with non-traditional EKF.

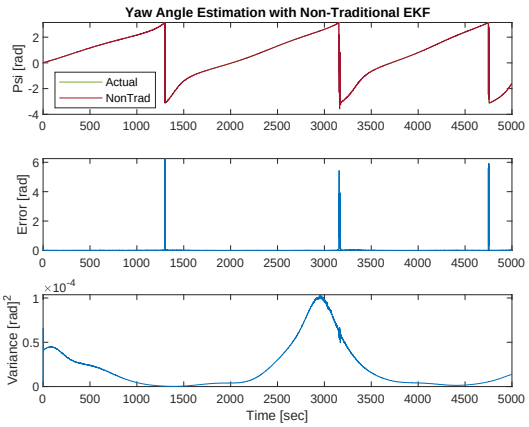

Figure 5.9 : Yaw angle estimation values with non-traditional EKF.

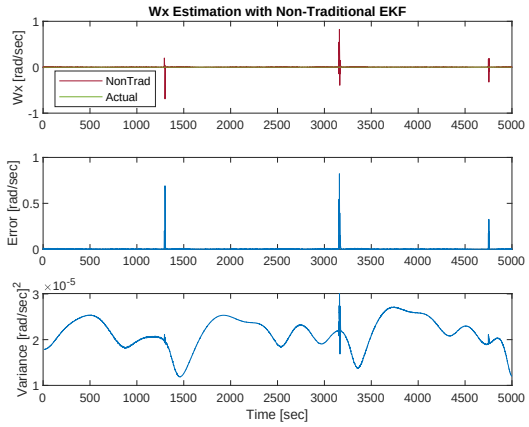

Figure 5.10 : ω_x estimation values with non-traditional EKF.

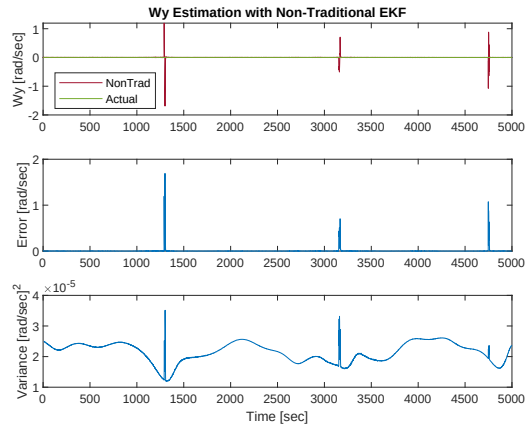

Figure 5.11 : ω_y estimation values with non-traditional EKF.

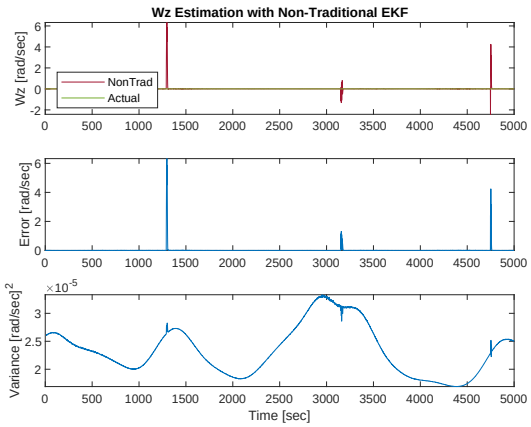

Figure 5.12 : ω_z estimation values with non-traditional EKF.

Because of an undetermined reason, there are seen jumps at some time steps which lead to be the graph unreadable properly. Thus, Chauvenet's criterion is applied to absolute error of the estimation values; and abnormal jumps are eliminated. The obtained graphs can be seen in Figure 5.13, 5.14, 5.15, 5.16, 5.17, and 5.18.

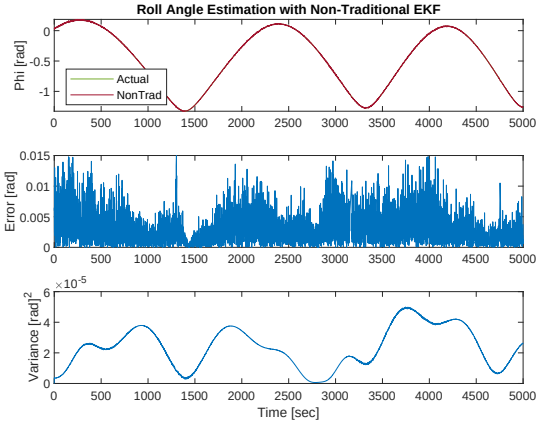

Figure 5.13 : Roll angle estimation values with non-traditional EKF.

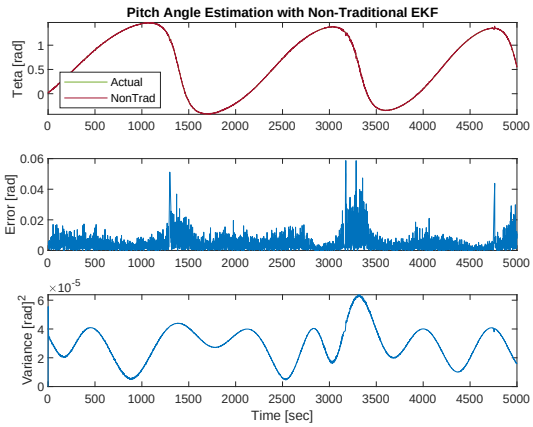

Figure 5.14 : Pitch angle estimation values with non-traditional EKF.

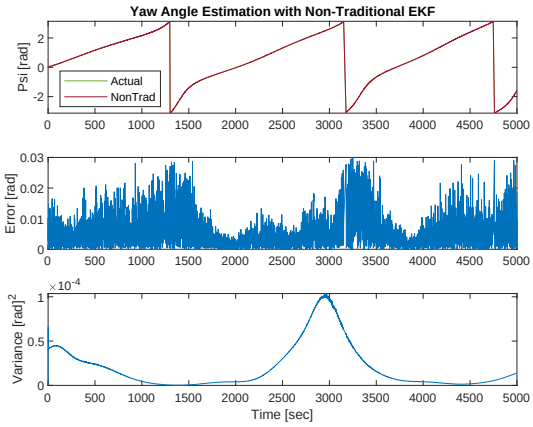

Figure 5.15 : Yaw angle estimation values with non-traditional EKF.

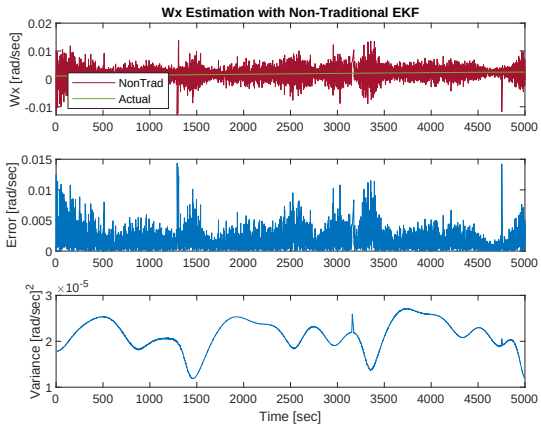

Figure 5.16 : ω_x estimation values with non-traditional EKF.

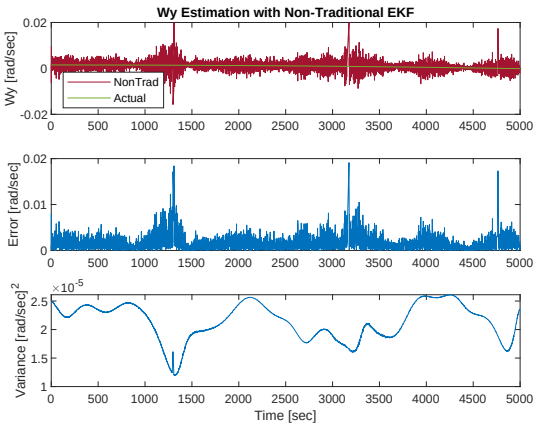

Figure 5.17 : ω_y estimation values with non-traditional EKF.

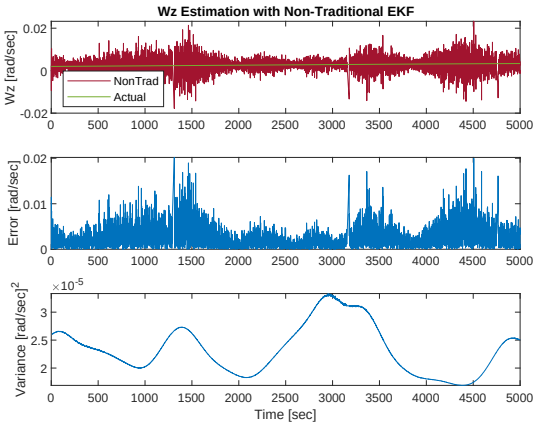

Figure 5.18 : ω_z estimation values with non-traditional EKF.

The results revealed that the non-traditional EKF with only TRIAD measurement works quite successful with errors lying within an acceptable range. However, even though it was expected to yield more accurate results compared to traditional EKF, due to an unidentified reason it resulted in worse estimations.

5.3 Non-Traditional EKF Estimations with TRIAD and ARES Measurements

The estimation results obtained by using non-traditional EKF with TRIAD and ARES measurements are given in Figures 5.19, 5.20, 5.21, 5.22, 5.23, and 5.24.

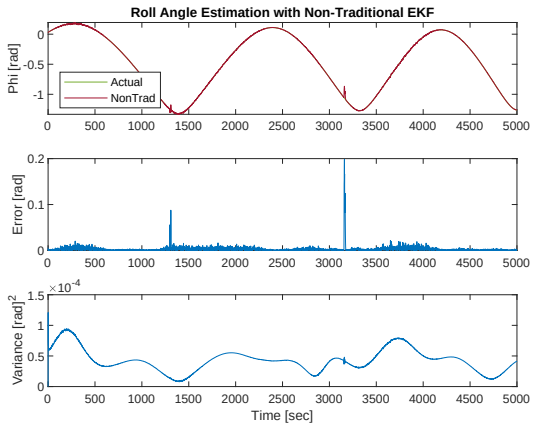

Figure 5.19 : Roll angle estimation values with non-traditional EKF.

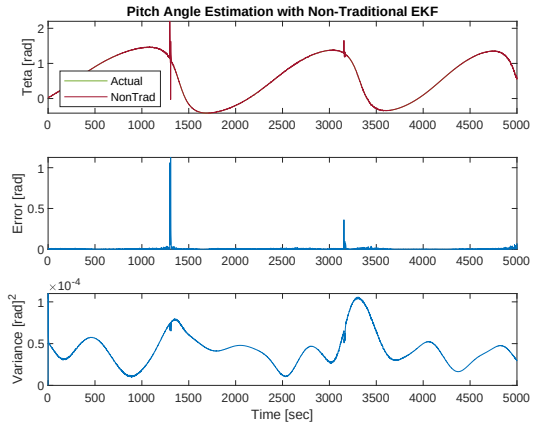

Figure 5.20 : Pitch angle estimation values with non-traditional EKF.

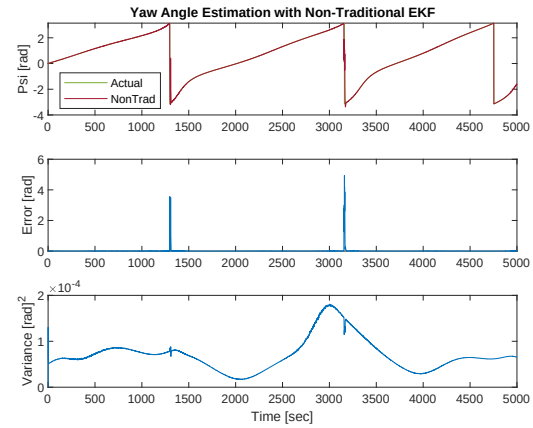

Figure 5.21 : Yaw angle estimation values with non-traditional EKF.

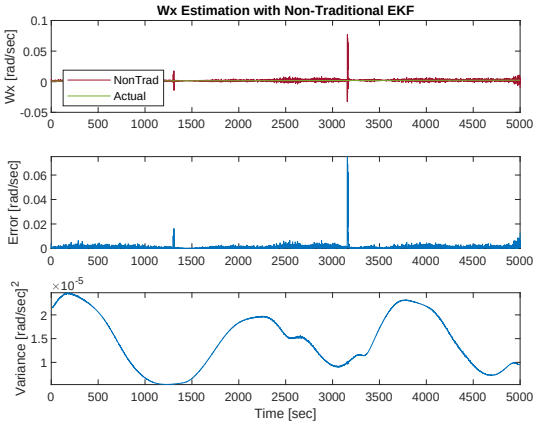

Figure 5.22 : ω_x estimation values with non-traditional EKF.

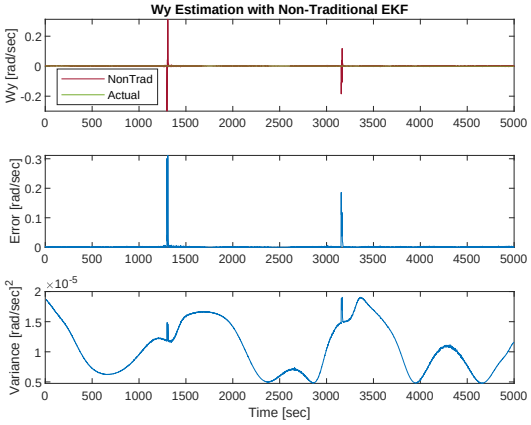

Figure 5.23 : ω_y estimation values with non-traditional EKF.

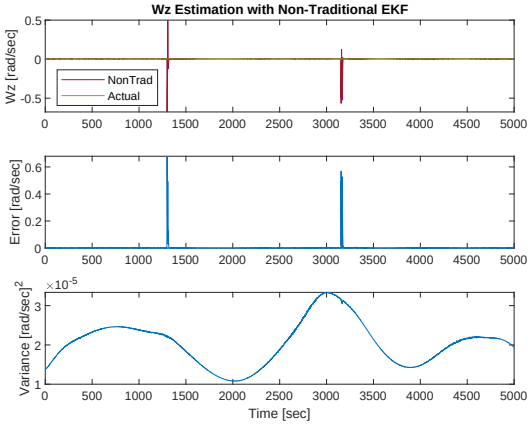

Figure 5.24 : ω_z estimation values with non-traditional EKF.

Similar to previous results, abnormal peaks were observed and to evaluate the accuracy of the method Chauvenet's criterion was applied again to eliminate these peaks. The

results obtained after Chauvenet's criterion are given in Figures 5.25, 5.26, 5.27, 5.28, 5.29, and 5.30.

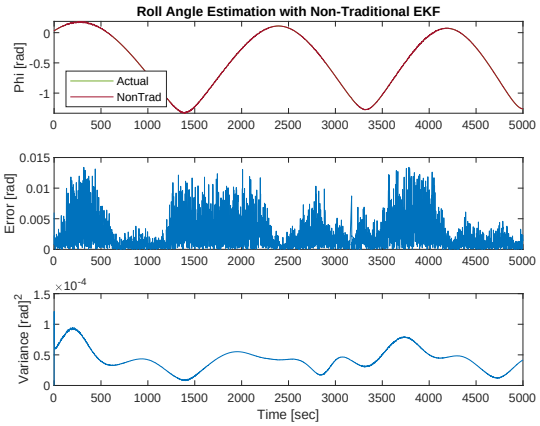

Figure 5.25 : Roll angle estimation values with non-traditional EKF.

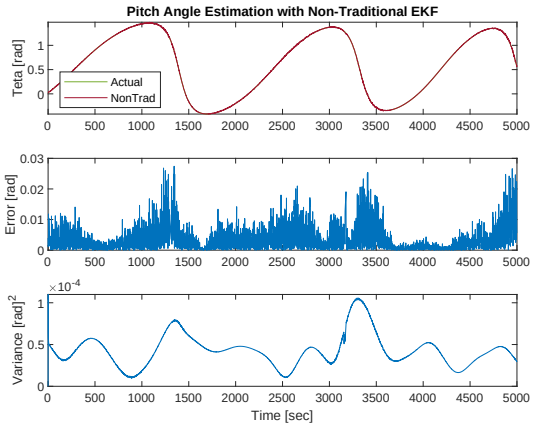

Figure 5.26 : Pitch angle estimation values with non-traditional EKF.

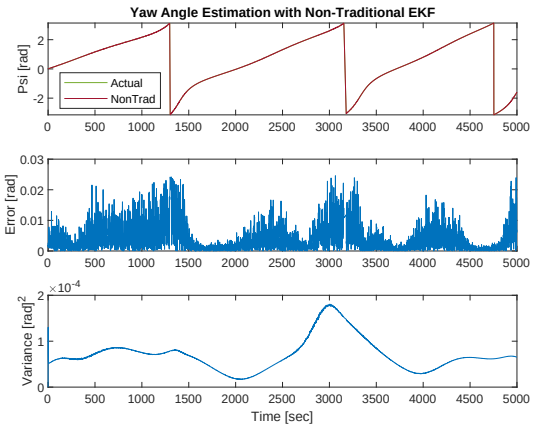

Figure 5.27 : Yaw angle estimation values with non-traditional EKF.

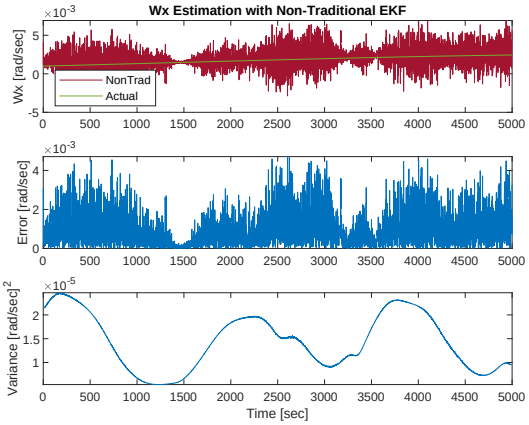

Figure 5.28 : ω_x estimation values with non-traditional EKF.

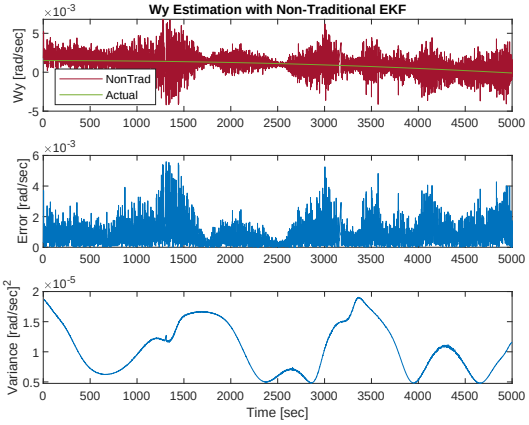

Figure 5.29 : ω_y estimation values with non-traditional EKF.

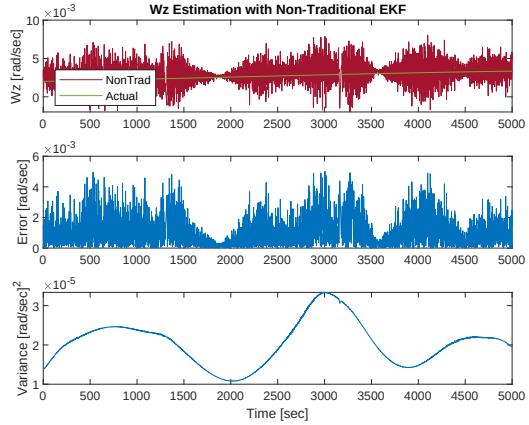

Figure 5.30 : ω_z estimation values with non-traditional EKF.

The results after Chauvenet's criterion indicates that this approach is also capable of estimating the state vectors accurately. The addition of ARES algorithm resulted in much better attitude angle and angular velocity estimations.

5.4 Traditional EKF Estimations with ARES Measurement

The estimation results obtained by using traditional EKF with ARES measurements are given in Figures 5.31, 5.32, 5.33, 5.34, 5.35, and 5.36.

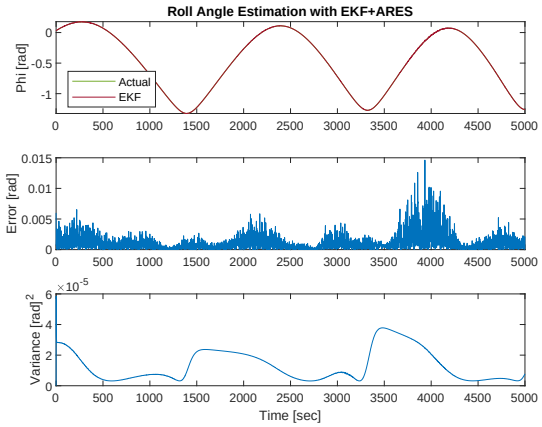

Figure 5.31 : Roll angle estimation values with traditional EKF.

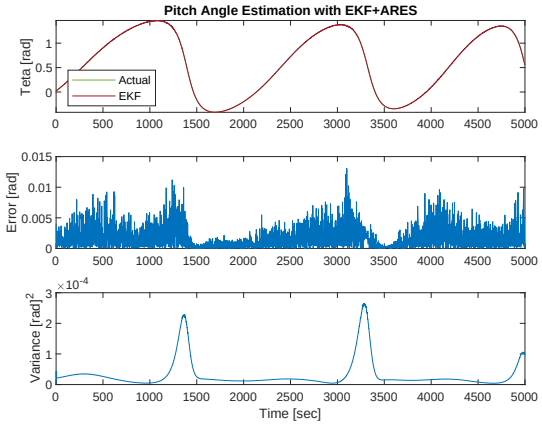

Figure 5.32 : Pitch angle estimation values with traditional EKF.

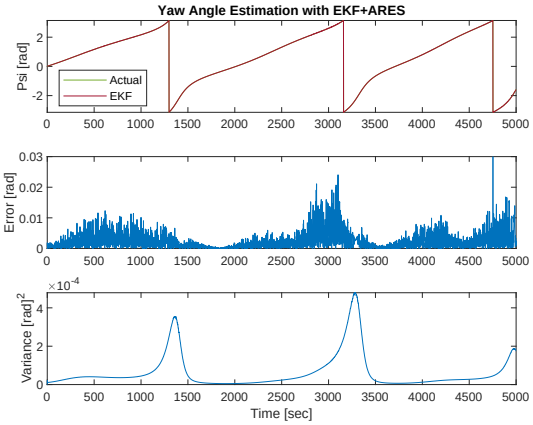

Figure 5.33 : Yaw angle estimation values with traditional EKF.

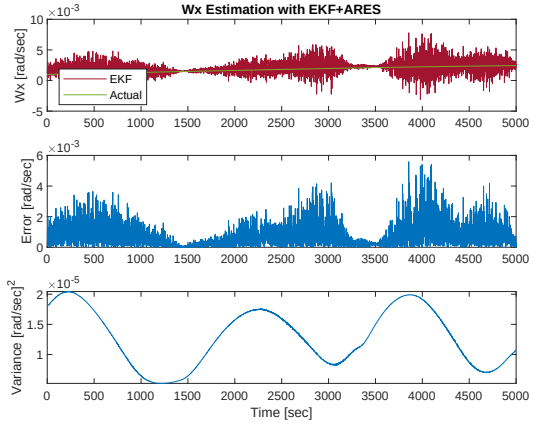

Figure 5.34 : ω_x estimation values with traditional EKF.

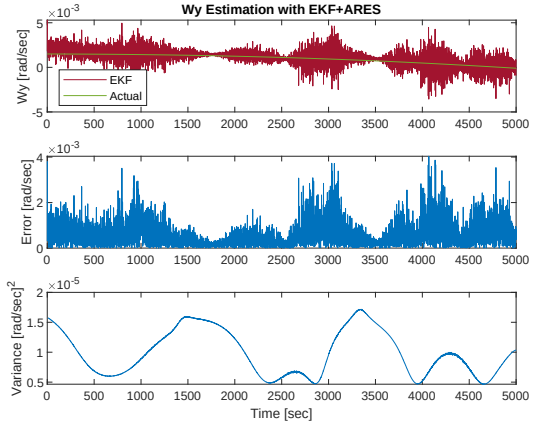

Figure 5.35 : ω_y estimation values with traditional EKF.

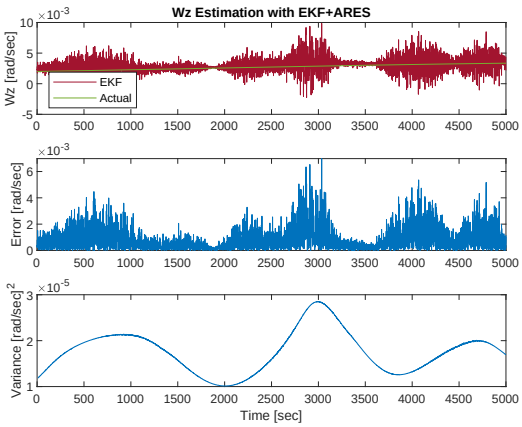

Figure 5.36 : ω_z estimation values with traditional EKF.

The results showed that integration of ARES measurements did not really change the accuracy of the attitude angles while slight improvements were observed in angular velocity estimations.

5.5 Comparison of Non-Traditional EKF Approaches

In this section, the results of non-traditional EKF estimations with TRIAD measurements and together with ARES measurements are compared. The comparison of the approaches was made using mean square error (MSE) and results are given in Table 5.1. Additionally, the estimation error values associated with the state vector components obtained with these approaches are given in Figures 5.37, 5.38, 5.39, 5.40, 5.41, and 5.42.

Table 5.1 : MSE analysis of non-traditional EKF.

Method	ϕ [rad]	θ [rad]	ψ [rad]	ω_x [rad/s]	ω_y [rad/s]	ω_z [rad/s]
TRIAD	0.0040	0.0059	0.0082	0.0023	0.0022	0.0038
TRIAD+ARES	0.0035	0.0051	0.0059	0.0013	0.0012	0.0014

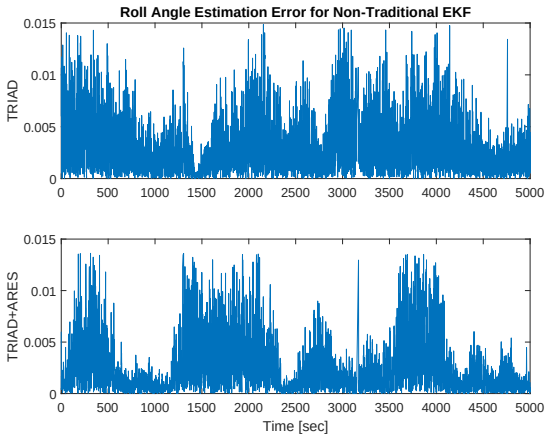

Figure 5.37 : Roll angle estimation value error.

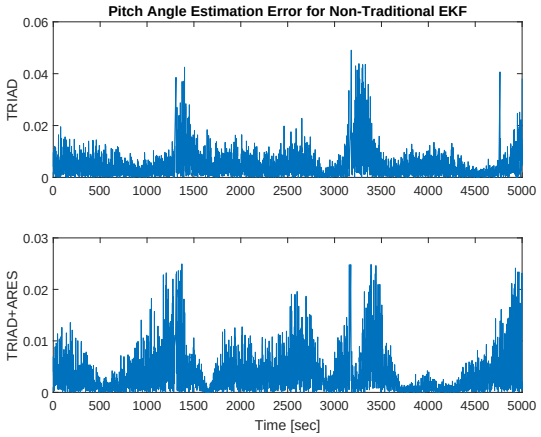

Figure 5.38 : Pitch angle estimation value error.

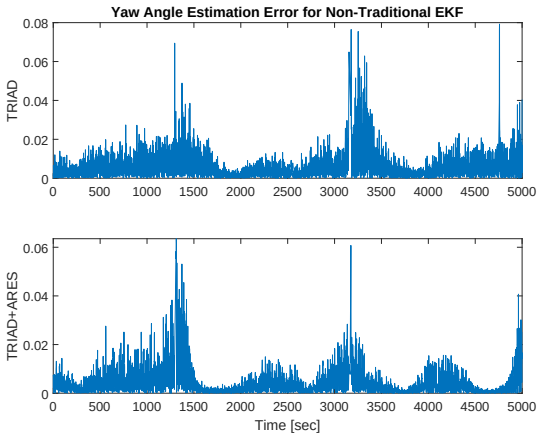

Figure 5.39 : Yaw angle estimation value error.

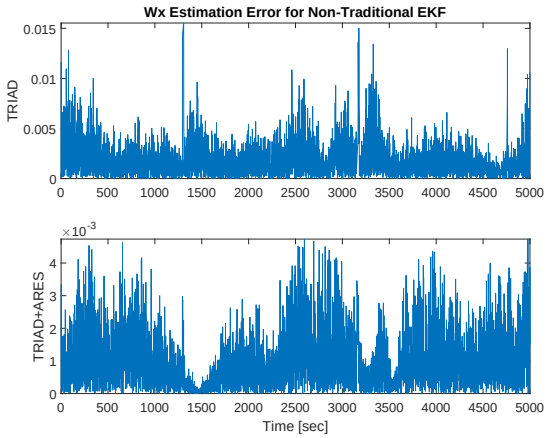

Figure 5.40 : ω_x estimation value error.

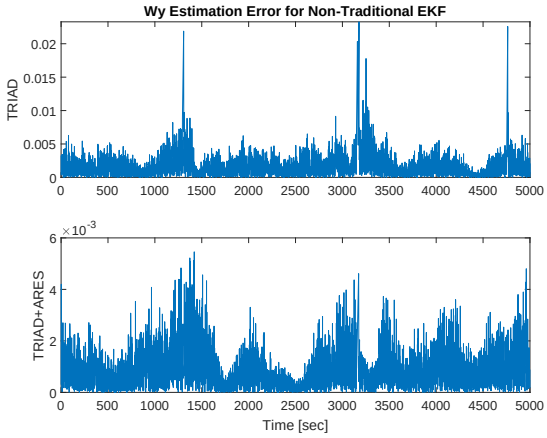

Figure 5.41 : ω_y estimation value error.

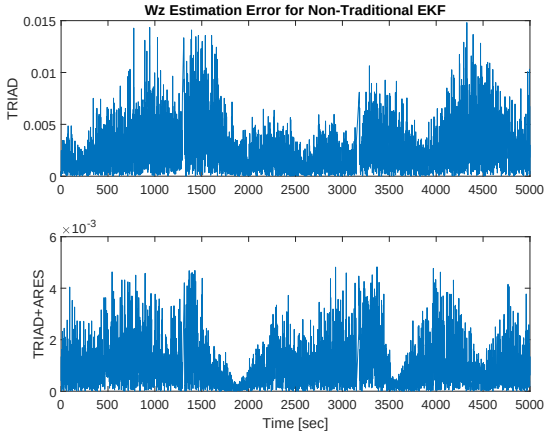

Figure 5.42 : ω_z estimation value error.

Based on the results, it was found that integration of ARES measurements to non-traditional EKF reduced the errors in all of the state vector components.

Especially, the error of the angular velocities were reduced to half while slight improvements were also seen in attitude angles.

5.6 Comparison of Traditional EKF and Non-Traditional EKF Approaches

In this section, a comparison between traditional EKF and non-traditional EKF with TRIAD measurements are made. The MSE comparison of two approaches' results are given in Table 5.2. Additionally, the estimation error values associated with the state vector components obtained with these approaches are given in Figures 5.43, 5.44, 5.45, 5.46, 5.47, and 5.48.

Table 5.2 : MSE analysis of traditional and non-traditional EKF.

Method	ϕ [rad]	θ [rad]	ψ [rad]	ω_x [rad/s]	ω_y [rad/s]	ω_z [rad/s]
EKF	0.0007	0.0012	0.0018	0.0005	0.0003	0.0006
Non-Trad	0.0040	0.0059	0.0082	0.0023	0.0022	0.0038

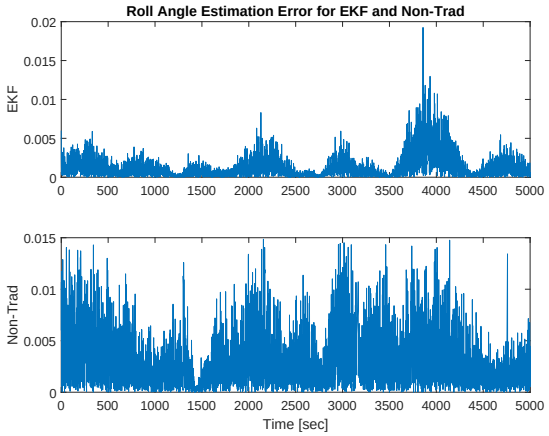

Figure 5.43 : Roll angle estimation value error.

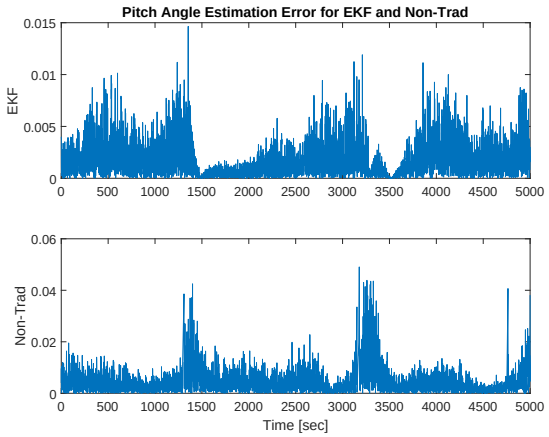

Figure 5.44 : Pitch angle estimation value error.

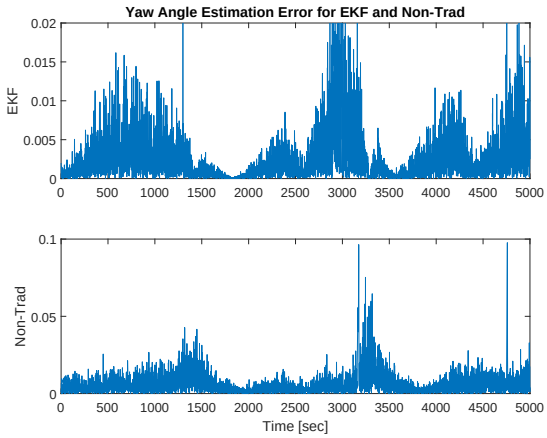

Figure 5.45 : Yaw angle estimation value error.

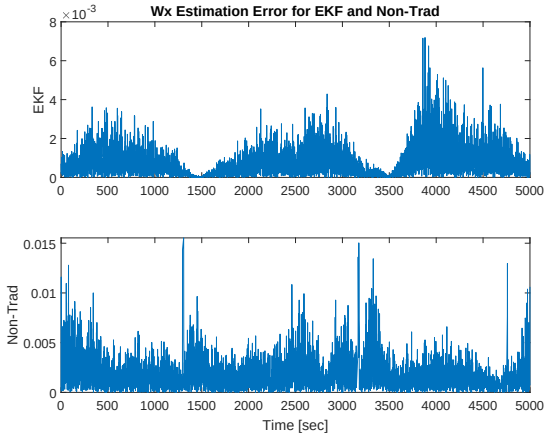

Figure 5.46 : ω_x estimation value error.

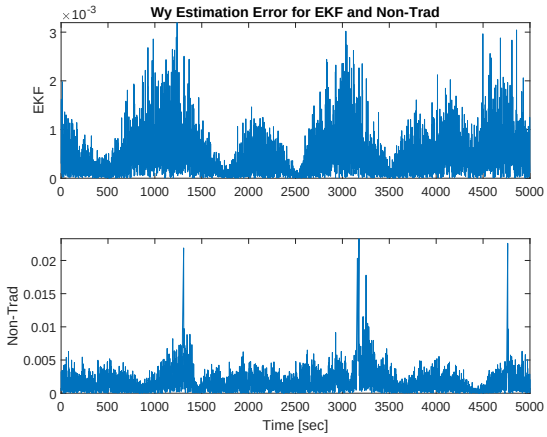

Figure 5.47 : ω_y estimation value error.

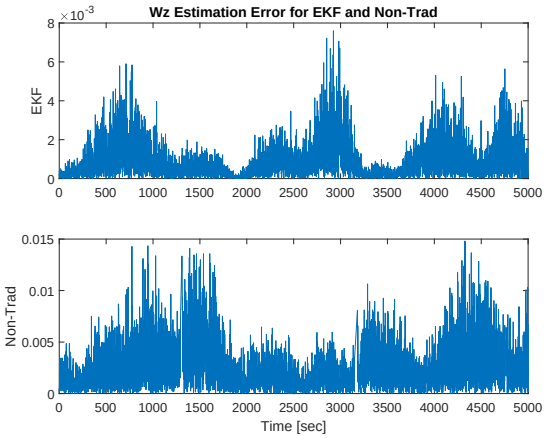

Figure 5.48 : ω_z estimation value error.

Contrary to expectations, utilization of non-traditional EKF with TRIAD measurements did not yield more accurate results than the traditional EKF results. This might be due to a few reasons which will be investigated in further details.

5.7 Comparison of Traditional EKF and Non-Traditional EKF Approaches with ARES Measurement

In this section, in order to see the effect of ARES measurements integration into both Kalman filter approaches a comparison was made. The MSE comparison results are given in Table 5.3. Additionally, the estimation error values associated with the state vector components obtained with these approaches are given in Figures 5.49, 5.50, 5.51, 5.52, 5.53, and 5.54.

Table 5.3 : MSE analysis of traditional and non-traditional EKF with ARES.

Method	ϕ [rad]	θ [rad]	ψ [rad]	ω_x [rad/s]	ω_y [rad/s]	ω_z [rad/s]
EKF	0.0007	0.0012	0.0016	0.0006	0.0004	0.0006
Non-Trad	0.0035	0.0051	0.0059	0.0013	0.0012	0.0014

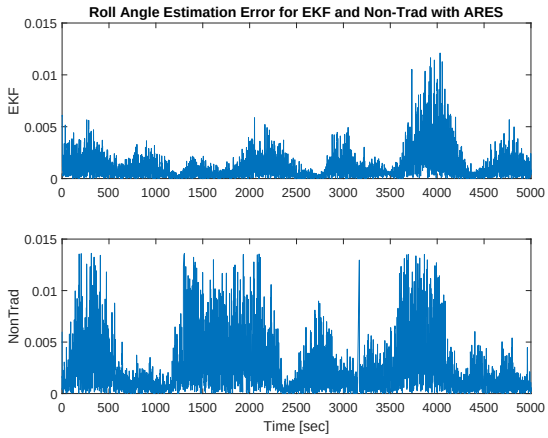

Figure 5.49 : Roll angle estimation value error.

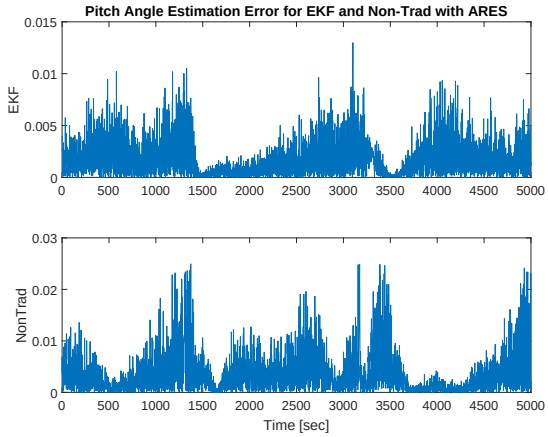

Figure 5.50 : Pitch angle estimation value error.

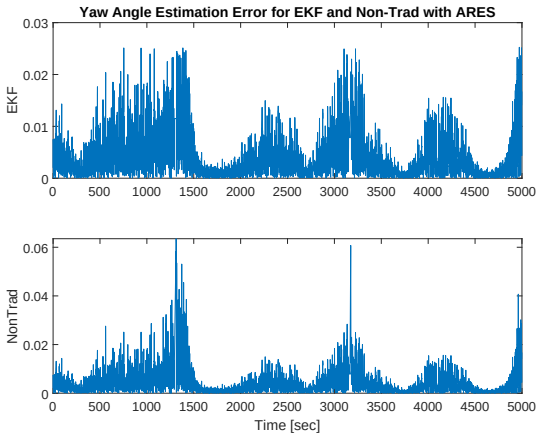

Figure 5.51 : Yaw angle estimation value error.

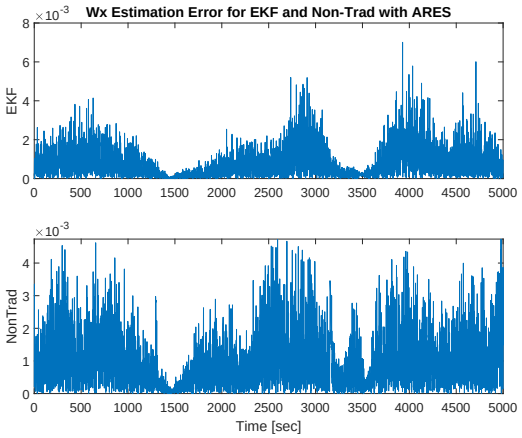

Figure 5.52 : ω_x estimation value error.

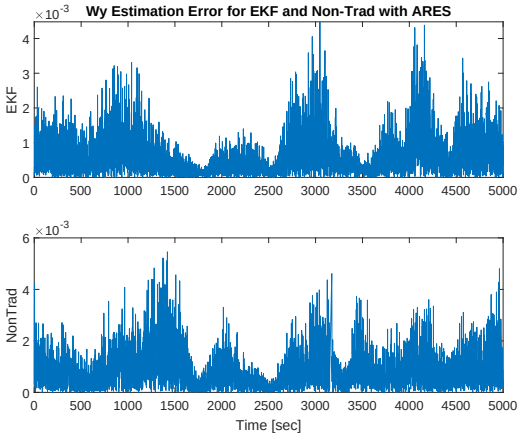

Figure 5.53 : ω_y estimation value error.

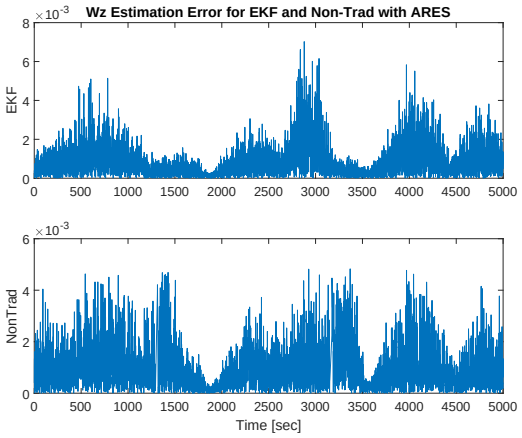

Figure 5.54 : ω_z estimation value error.

The result given in the Table 5.3 revealed that even with the integration of ARES measurement the non-traditional EKF was not as successful as the traditional EKF.

Nevertheless, the improvement achieved by the integration of ARES measurement into the non-traditional EKF was greater than that of the traditional EKF. Considering this fact, it may be presumed that utilization of additional measurement data might enhanced the non-traditional EKF even further than the traditional EKF.

6. FAULT TOLERANT ATTITUDE DETERMINATION

6.1 Fault Modeling and Residual Generation

6.1.1 Sensor fault modeling

Sensor faults are generally modeling with fault addition in the AD system within the corresponding measurement equation [46]. Since the sensor failures are independent of the system dynamic behavior, additive changes are generally valid. For a linear time-varying system, the equations, with failure (γ_1) and without failure (γ_0), are given as follows:

$$\gamma_0 : z(t_k) = Hx(t_k) + v(t_k) \tag{6.1}$$

$$\gamma_1 : z(t_k) = Hx(t_k) + v(t_k) + L_j S_{t_k - \tau^*} \nu \tag{6.2}$$

where x, z, and v denote the state, the measurement, and the disturbance. Furthermore, L_j expresses how the failure is introduced to the system while S_{t_k} indicates the *failure mode*. ν and τ^* represent the magnitude of the unknown failure and its occurring time step, respectively.

6.1.2 Residual processing

The REKF creates a critical knowledge named as residual which is mostly used to detect failure through statistically analyze the residuals and to identify the faulty components.

The REKF is developed to be used for the FDI system, in order to produce residuals and achieve the state estimation with help of the measured observations passing through the filter. The REKF algorithm calculates the residuals by subtracting the state information measured by sensor, z^*, from the estimated values which established by the REKF, $\hat{z}$,

$$e = Resx = z^* - \hat{z} \tag{6.3}$$

The effective characteristics of the residual can be listed as its zero-mean (without fault) and white (independent) properties. These characteristics stimulates its use as a quantity to imply the presence of faults and can come in handy when developing a health monitoring scheme for the AD system of a pico satellite.

Generally, the residuals are generated by addition of two components which are the noise and the faults. The noise can be expressed as a random quantity with zero-mean while the faults are deterministic and unknown. Therefore, the residuals are random variables, mean of which is dominated by the faults. This drives to defining the detection issue as one of examining the zero-mean hypothesis. The consideration of an isolation issue leads to a decision making process between different hypotheses.

6.1.3 Chi-square test

The most commonly used method to examine a change in the mean value of a random vector is the chi-square test which is a statistical hypotheses testing method [47]. For fault detection purposes, the chi-square test is applied to the residuals where it decides if a fault is present or not. A null hypothesis γ_0 is defined for the no-fault case and a hypothesis γ_1 is defined for the non-zero mean of the residual, indicating the presence of a fault. These hypotheses are given as follows:

$$\gamma_0 : \beta(t_k) \leqslant \chi^2_{\alpha,s}, \quad \forall t_k \tag{6.4}$$

$$\gamma_1 : \beta(t_k) > \chi^2_{\alpha,s}, \quad \exists t_k \tag{6.5}$$

Then, the statistical function $\beta(t_k)$ is formed with vector $e(t_k)$ as follows:

$$\beta(t_k) = e^T(t_k) V_e^{-1}(t_k) e(t_k) \tag{6.6}$$

where V_e is the covariance of the residuals which are estimated by filters according to

$$V_e(t_{k+1}) = H(t_{k+1}) P(t_{k+1}|t_k) H^T(t_{k+1}) + R(t_{k+1}) \tag{6.7}$$

In the health monitoring applications, the main reason of the application of the chi-square test is to create a warning. However, it does not aim for isolating the failures. Properly selected thresholds create an impact by avoiding false alarm signals and noting actual faults rather than overlooking. The scheme developed here, attempts to minimize the chances of overlooking the actual faults with proper selection of threshold and implementation of the steps of detection.

6.2 Development of the FDI System

In this section, FDI of the AD system of a spacecraft is considered and a system based on REKF and residual processing by statistical and hypotheses testing is developed. The developed FDI module detects and isolates any faults within the on-board sensor, measurements of which are processed for AD purposes. In this way, the FDI module implies that a sensor is failed based on the collected information and as a result of that MNSF can be set to a certain value for recovery actions.

The FDI system developed in this study has two main phases, namely fault detection and fault isolation. The residuals generated by the REKF is used in these two phases of the algorithm. The following sections explain the phases of the system and they are discussed in detail.

6.2.1 Fault detection

The fault detection is the first phase of the FDI and it detects any unknown faults. Statistical threshold tests are constantly used to check the residuals and see whether they exceed the defined threshold. If the thresholds are violated, then a failure is declared. For statistical threshold test - the chi-square test - is applied to the residuals generated by the REKF.

6.2.2 Fault isolation

The second phase in the FDI system aims to isolate a detected failure while trying to figure out which magnetometer causes it. This can be achieved by calculating the normalized innovations as follows:

$$InN(t_{k+1}) = (\sqrt{V_e(t_{k+1})})^{-1} e(t_{k+1}) \tag{6.8}$$

The normalized innovation indicates the failure for a failed magnetometer while the normalized innovation values remain unchanged for healthy sensors. Thus, the sensor with failure can easily be identified. For a case where all the normalized innovation values imply a fault, the source of failure can be identified as all of the sensors.

6.3 Robust EKF Algorithm

Under such conditions where no fault is present, it is expected to obtain very good estimation results with the implementation of the EKF. However, in real life such conditions are rare to encounter. If any of the measurements are faulty due to abnormalities or sharp deviations in the measurement channel, the application of the EKF would yield inferior estimations. This highlights the need of a better working algorithm that can tolerate any fault within the system.

REKF algorithm is designed to tolerate faulty measurements without compromising the accuracy of the estimations. The fundamental idea behind the REKF is to make a comparison between the real and the theoretical values of the covariance matrices. When there are large differences between the theoretical and real values, the Kalman filter gain adapts itself accordingly. For such cases, the covariance matrix of the innovation changes in a way as follows:

$$V_e(t_{k+1}) = H(t_{k+1}) P(t_{k+1}|t_k) H^T(t_{k+1}) + S(t_k) R(t_{k+1}) \tag{6.9}$$

resulting in the Kalman filter as

$$K(t_{k+1}) = P(t_{k+1}|t_k) H^T(t_{k+1}) \times [H(t_{k+1}) P(t_{k+1}|t_k) H^T(t_{k+1}) + S(t_k) R(t_{k+1})]^{-1} \tag{6.10}$$

where $H(t_{k+1})$, $P(t_{k+1}|t_k)$, $S(t_k)$, $R(t_{k+1})$, and $K(t_{k+1})$ denote the measurement matrix, the predicted covariance matrix, the measurement noise scale factor, the covariance matrix of the measurement noise, and the Kalman gain, respectively.

By definition, the Kalman gain changes when the predicted observation, $H(t_{k+1})\hat{x}(t_{k+1}|t_k)$, differs significantly from the actual observation, $y(t_{k+1})$, due to

momentous changes in the operational conditions. If the real value of filter error is bigger than the expected error represented as

$$tr\{e(t_{k+1})e^T(t_{k+1})\} => tr\{H(t_{k+1})P(t_{k+1}|t_k)H^T(t_{k+1}) + R(t_{k+1})\} \tag{6.11}$$

REKF must be used rather than EKF, where $tr\{.\}$ stands for the trace of the regarding matrix.

To obtaion the scale factor, $S(t_k)$, equation 6.9 can be substituted into 6.11 when the condition 6.11 is satisfied,

$$tr\{e(t_{k+1})e^T(t_{k+1})\} = tr\{H(t_{k+1})P(t_{k+1}|t_k)H^T(t_{k+1})\} + S(t_k)tr\{R(t_{k+1})\} \tag{6.12}$$

Considering the $tr\{e(t_{k+1})e^T(t_{k+1})\} = e^T(t_{k+1})e(t_{k+1})$ equality, $S(t_k)$ can be obtained as follows:

$$S(t_k) = \frac{e^T(t_{k+1})e(t_{k+1}) - tr\{H(t_{k+1})P(t_{k+1}|t_k)H^T(t_{k+1})\}}{tr\{R(t_{k+1})\}} \tag{6.13}$$

When a fault is present in the measurement system, the adaptation of the EKF can be performed by correcting the Kalman gain automatically. If the condition given in Equation 6.11 is met, then the scale factor, $S(t_k)$ increases. The higher the scale factor is, smaller than Kalman gain in equation 6.10 becomes due to the covariance of the innovation sequence given in 6.9. As a result of that, the effect of the faulty innovation sequence on the state estimation process decreases due to small Kalman gain. Otherwise, when the measurement system operates normally, the scale factor takes the value of 1, indicating optimal run of the filter.

One important thing to mention here is that the scale factor, $S(t_k)$ has an adverse effect on the estimation error covariance which gets higher in the REKF beside the EKF. Therefore, it is suggested that the utilization of the REKF should only be carried out when the system has faulty measurements. All the other cases should implement the regular EKF in order to achieve accurate estimations.

The simulations are realized with given conditions in Section 5 in the presence of a fault between 1000th and 1500th seconds. First, the results obtained by the traditional EKF approach are shown and discussed.

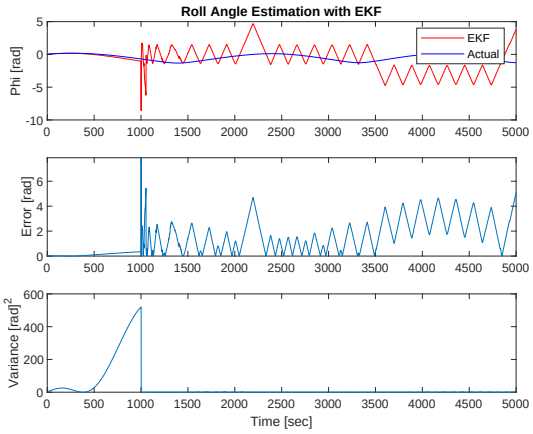

Figure 6.1 : Roll angle estimation values with EKF.

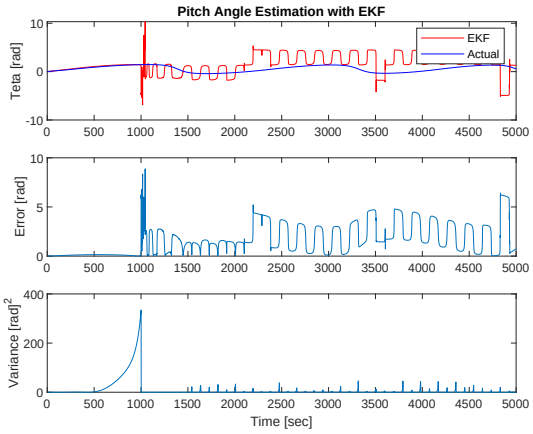

Figure 6.2 : Pitch angle estimation values with EKF.

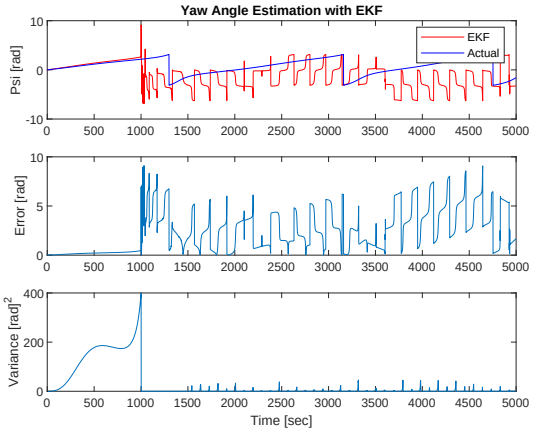

Figure 6.3 : Yaw angle estimation values with EKF.

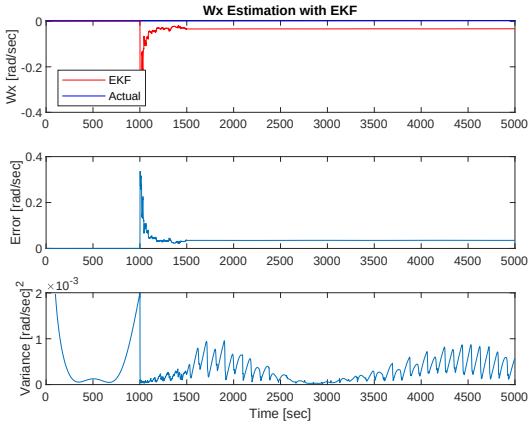

Figure 6.4 : ω_x estimation values with EKF.

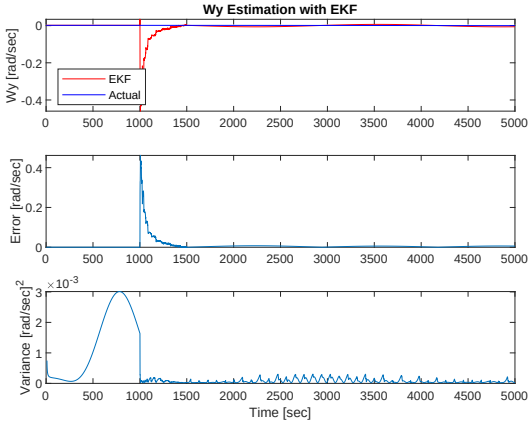

Figure 6.5 : ω_y estimation values with EKF.

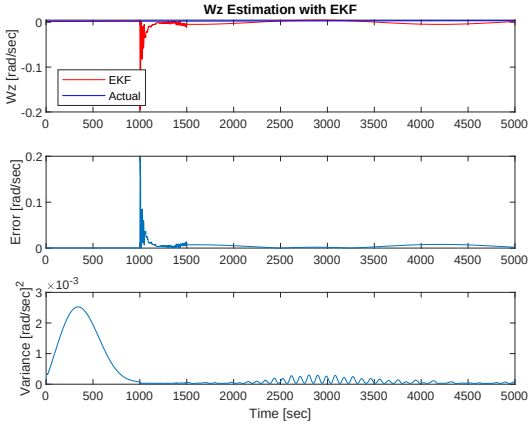

Figure 6.6 : ω_z estimation values with EKF.

The EKF results showed that in the presence of a fault between the specified time interval, the algorithm was not capable of compensating for the fault. Thus, it was

observed that the results did not agree well with the actual values, which was an anticipated behavior. Then, the same case was addressed with the REKF algorithm and the results are presented and discussed below.

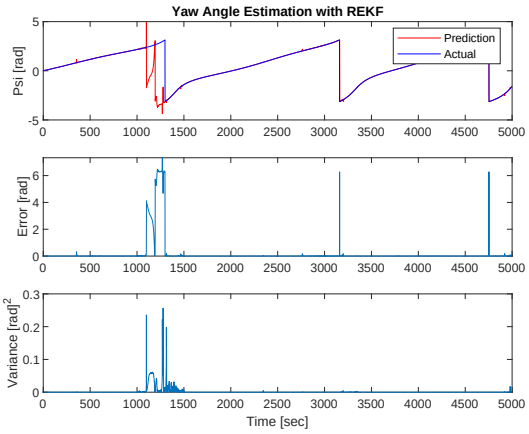

Figure 6.7 : Roll angle estimation values with REKF.

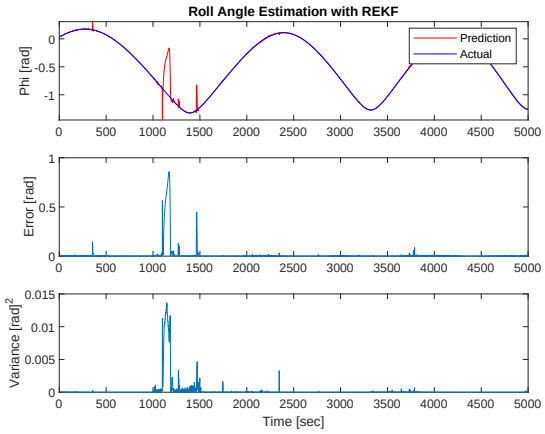

Figure 6.8 : Pitch angle estimation values with REKF.

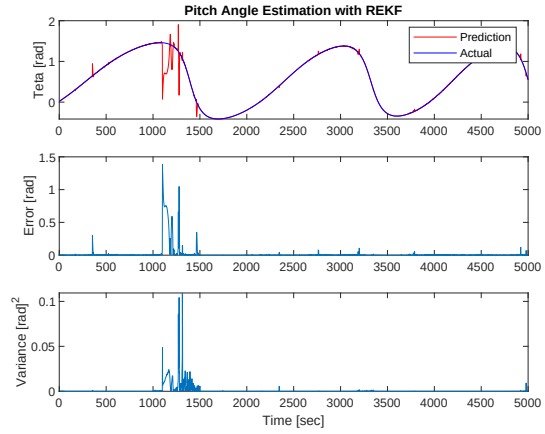

Figure 6.9 : Yaw angle estimation values with REKF.

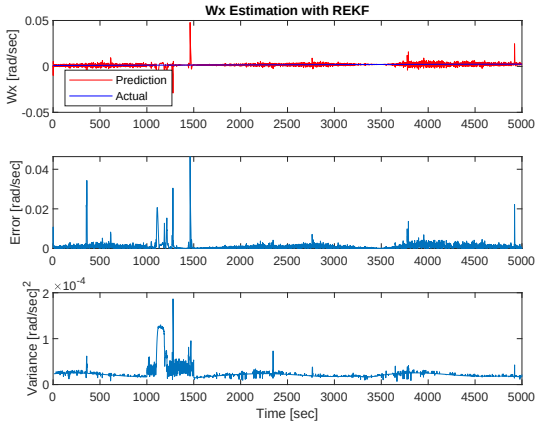

Figure 6.10 : ω_x estimation values with REKF.

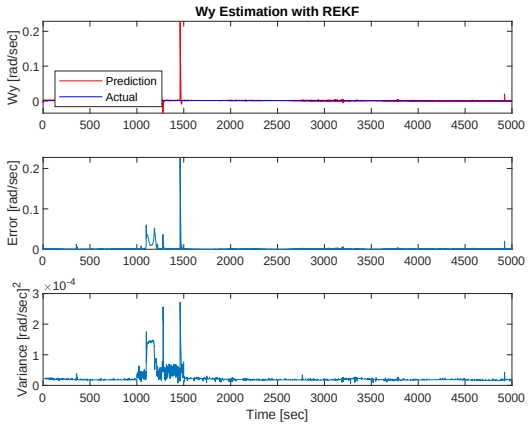

Figure 6.11 : ω_y estimation values with REKF.

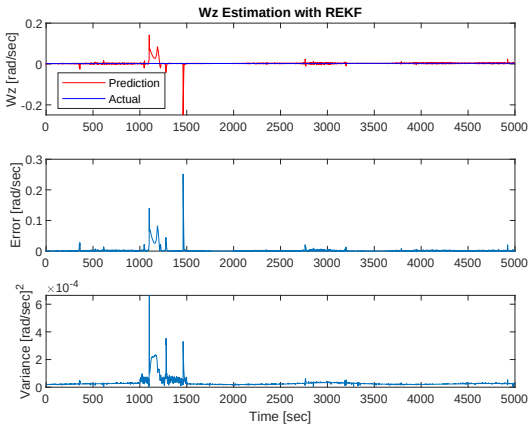

Figure 6.12 : ω_z estimation values with REKF.

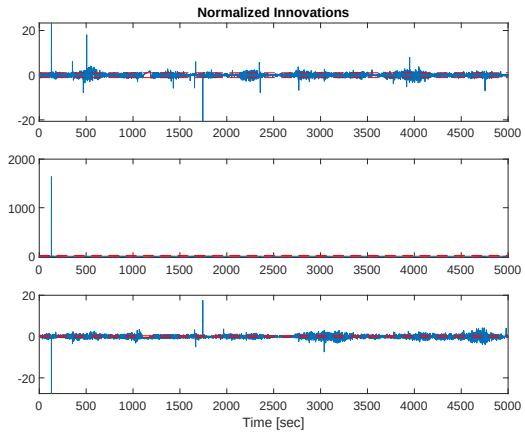

Figure 6.13 : Normalized innovations.

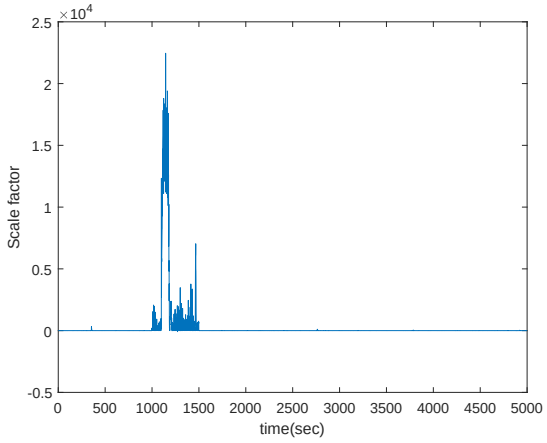

Figure 6.14 : Scale factor.

These results indicated that the REKF algorithm was able to work properly in terms of detecting and recovering the faults introduced to the system.

7. CONCLUSIONS

The estimated Euler angles are generated by using two vector algorithm and TRIAD. Since the resulting graphs of the two methods are tracing similar trends, it can be said that both of them are suitable for using in these analysis. The two methods have different error finding for different kind of Euler angle estimation process. Thus, the evaluation of which one is better for estimating Euler angles can not be made sharply. The covariance analysis also be done and it is decided that the results are in proper ranges.

Angular velocity estimations have been executed using the method proposed by [41]. In the original method, there are used only star sensor measurements with a changing number of star vectors for calculation. Since the star sensor are more accurate than the sun sensor and the magnetometer, the estimated angular velocity values could not catch the real data. However, when the variance graph are investigated, it is seen that the error values are increasing at the covariance graph pick points. Therefore, it can be said that the overall algorithm is implemented successfully.

In order to determine the attitude angles, an EKF algorithm collecting measurement data from a magnetometer and a sun sensor was implemented. To overcome the nonlinearity within the measurement model and linearize it, the nontraditional approach was applied. As a result of this application, a nontraditional EKF which uses the TRIAD results as the measurement model was developed. For angular velocity prediction, ARES results were integrated to the classical and nontraditional approaches as a secondary measurement model, and the simulation results were compared. Based on the simulation results, it was found that ARES and TRIAD aided nontraditional EKF works more accurately than TRIAD-aided nontraditional EKF method. Furthermore, a comparison between classical EKF and TRIAD aided nontraditional EKF yielded that surprisingly, classical EKF is the superior one in this case. Finally, the results also revealed that ARES-aided EKF works better than ARES and TRIAD aided nontraditional EKF algorithm. Based on the simulation results, it

is seen that enhancement in the measurement vector of the nontraditional EKF gives better response compared with the traditional EKF approach. Thus, it can be concluded that increasing the accuracy of the measurement used in the nontraditional EKF has the potential of yielding more accurate results than the traditional EKF.

In order to verify the REKF algorithm, a fault is introduced to one of the measurements taken by the magnetometer. The fault basically modifies the magnetometer measurement by a constant term, either addition or subtraction. The fault is inserted to the system between the time steps of 1000 and 1500 sec of the simulations. The comparison between the state estimation and real data has shown that even in the presence of a faulty sensor, the REKF was able to detect the fault and compensate it with an acceptable accuracy.

REFERENCES

[1] **Trishchenko, A.P. and Garand, L.** (2012). Observing polar regions from space: advantages of a satellite system on a highly elliptical orbit versus a constellation of low Earth polar orbiters, *Canadian Journal of Remote Sensing*, *38*(1), 12–24.

[2] **Kyle, O.** (2001). Availability and reliability advantages of GPS/Galileo integration, *Proceedings of ION GPS 2001, Session C4, Salt Lake City, UT*.

[3] **Yesou, H.**, **Clandillon, S.**, **Allenbach, B.**, **Bestault, C.**, **De Fraipont, P.**, **Inglada, J. and Favard, J.** (2003). A constellation of advantages with SPOT SWIR and VHR SPOT 5 data for flood extent mapping during the September 2002 Gard event (France), *IGARSS 2003. 2003 IEEE International Geoscience and Remote Sensing Symposium. Proceedings (IEEE Cat. No. 03CH37477)*, volume 1, IEEE, pp.567–569.

[4] **Qu, Z.**, **Zhang, G.**, **Cao, H. and Xie, J.** (2017). LEO satellite constellation for Internet of Things, *IEEE Access*, *5*, 18391–18401.

[5] **Houyou, A.**, **Holzer, R.**, **Meer, H. and Heindl, M.** (2005). Performance of transport layer protocols in LEO pico-satellite constellations, *University of Passau, Passau, Germany, MIP-0502*.

[6] **Hamann, R.**, **Verhoeven, C.J. and Bonnema, A.** (2005). Nano-satellites, a fast way to pre-qualify new micro-technology, *2005 International Conference on MEMS, NANO and Smart Systems*, IEEE, pp.263–264.

[7] **Kayal, H. and Briess, K.** (2011). Pico Satellite Concept of Tu-Berlin, *Small Satellites for Earth Observation: Selected Proceedings of the 5th International Symposium of the International Academy of Astronautics, Berlin, April 4-8 2005*, Walter de Gruyter, p.410.

[8] **Candini, G.P.**, **Piergentili, F. and Santoni, F.** (2012). Miniaturized attitude control system for nanosatellites, *Acta Astronautica*, *81*(1), 325–334.

[9] **Fujiwara, K.**, **Omagari, K.**, **Iljic, T.**, **Masumoto, S.**, **Konda, Y.**, **Yamanaka, T.**, **Tanaka, Y.**, **Maeno, M.**, **Ueno, T.**, **Ashida, H.** *et al.* (2007). Tokyo Tech nano-satellite Cute-1.7+ APD flight operation results and the succeeding satellite, *IFAC Proceedings Volumes*, *40*(7), 732–737.

[10] **Reichel, F.**, **Bangert, P.**, **Busch, S.**, **Ravandoor, K. and Schilling, K.** (2013). The attitude determination and control system of the picosatellite uwe-3, *IFAC Proceedings Volumes*, *46*(19), 271–276.

[11] **Ke, H.**, **Hao, W.**, **Binjie, T. and Zhonghe, J.** (2011). Pico-satellite autonomous navigation with magnetometer and sun sensor data, *Chinese Journal of Aeronautics*, *24*(1), 46–54.

[12] **Markley, F.L. and Crassidis, J.L.** (2014). *Fundamentals of spacecraft attitude determination and control*, volume 33, Springer.

[13] **Wertz, J.R.** (2012). *Spacecraft attitude determination and control*, volume 73, Springer Science & Business Media.

[14] **Cilden Guler, Demet & Hajiyev, C.** (2017). *Gyroless Attitude Determination of Nanosatellites Single-Frame Methods and Kalman Filtering Approach*, LAP LAMBERT Academic Publishing.

[15] **Cilden-Guler, D.**, **Soken, H.E. and Hajiyev, C.** SVD-Aided UKF for Estimation of Nanosatellite Rotational Motion Parameters.

[16] **Hajiyev, C.**, **Soken, H.E. and Cilden-Guler, D.** (2019). Nontraditional Attitude Filtering with Simultaneous Process and Measurement Covariance Adaptation, *Journal of Aerospace Engineering*, *32*(5), 04019054.

[17] **Hinks, J.C. and Psiaki, M.L.** (2011). Solution Strategies for an Extension of Wahba's Problem to a Spinning Spacecraft, *Journal of guidance, control, and dynamics*, *34*(6), 1734–1745.

[18] **Markley, F.L. and Mortari, D.** (2000). Quaternion attitude estimation using vector observations., *Journal of the Astronautical Sciences*, *48*(2), 359–380.

[19] **Çilden, D.**, (2016), Investigation and Development of Nontraditional Approach for Attitude Estimation of Small Satellites.

[20] **Markley, F.L.**, **Crassidis, J. and Cheng, Y.** (2005). Nonlinear attitude filtering methods, *AIAA Guidance, Navigation, and Control Conference and Exhibit*, p.5927.

[21] **Psiaki, M.L.**, **Huang, L. and Fox, S.M.** (1993). Ground tests of magnetometer-based autonomous navigation (MAGNAV) for low-earth-orbiting spacecraft, *Journal of Guidance, Control, and Dynamics*, *16*(1), 206–214.

[22] **Shorshi, G. and Bar-Itzhack, I.Y.** (1995). Satellite autonomous navigation based on magnetic field measurements, *Journal of Guidance, Control, and Dynamics*, *18*(4), 843–850.

[23] **Wiegand, M.** (1996). Autonomous satellite navigation via Kalman filtering of magnetometer data, *Acta Astronautica*, *38*(4-8), 395–403.

[24] **Deutschmann, J.K. and Bar-Itzhack, I.Y.** (2001). Evaluation of attitude and orbit estimation using actual earth magnetic field data, *Journal of Guidance, Control, and Dynamics*, *24*(3), 616–623.

[25] **Rong, S.**, **Mu, R. and Cui, N.** (2006). A fault tolerant filter applied on magnetometer-based autonomous satellite navigation, *2006 1st International Symposium on Systems and Control in Aerospace and Astronautics*, IEEE, pp.4–pp.

[26] **Psiaki, M.L.**, **Martel, F. and Pal, P.K.** (1990). Three-axis attitude determination via Kalman filtering of magnetometer data, *Journal of Guidance, Control, and Dynamics*, *13*(3), 506–514.

[27] **Sekhavat, P.**, **Gong, Q. and Ross, I.M.** (2007). NPSAT1 parameter estimation using unscented kalman filtering, *2007 American Control Conference*, IEEE, pp.4445–4451.

[28] **Soken, H. and Hajiyev, C.** (2008). Unscented Kalman filter based attitude estimation of ITU-PSAT I satellite using magnetometer measurements, *Proc. of the International Workshop on Small Satellites, New Missions and New Technologies*, pp.72–76.

[29] **Hajiyev, C. and Bahar, M.** (2001). Multichannel Kalman filter based on preliminary data compression for the satellite rotational motion parameters identification, *Third International Conference on Nonlinear Problems in Aviation and Aerospace, Daytona Beach, FL*, pp.277–284.

[30] **Hajiyev, C. and Bahar, M.** (2003). Attitude determination and control system design of the ITU-UUBF LEO1 satellite, *Acta Astronautica*, *52*(2-6), 493–499.

[31] **Cordova-Alarcon, J.R.**, **Mendoza-Barcenas, M.A. and Solis-Santome, A.**, (2015). Attitude Determination System Based on Vector Observations for Satellites Experiencing Sun-Eclipse Phases, Multibody Mechatronic Systems, Springer, pp.75–85.

[32] **Jiang, J.** (2005). Fault-tolerant control systems-an introductory overview, *Acta Automatica Sinica*, *31*(1), 161–174.

[33] **Hwang, I.**, **Kim, S.**, **Kim, Y. and Seah, C.E.** (2009). A survey of fault detection, isolation, and reconfiguration methods, *IEEE transactions on control systems technology*, *18*(3), 636–653.

[34] **Pirmoradi, F.**, **Sassani, F. and De Silva, C.** (2009). Fault detection and diagnosis in a spacecraft attitude determination system, *Acta Astronautica*, *65*(5-6), 710–729.

[35] **Chen, X.**, **Sun, R.**, **Jiang, W.**, **Jia, Q. and Zhang, J.** (2016). A novel two-stage extended Kalman filter algorithm for reaction flywheels fault estimation, *Chinese Journal of Aeronautics*, *29*(2), 462–469.

[36] **Mehra, R.**, **Seereeram, S.**, **Bayard, D. and Hadaegh, F.** (1995). Adaptive Kalman filtering, failure detection and identification for spacecraft attitude estimation, *Proceedings of International Conference on Control Applications*, IEEE, pp.176–181.

[37] **Soken, H.E. and Hacizade, C.** (2019). Tuning the Attitude Filter: A Comparison of Intuitive and Adaptive Approaches, *2019 9th International Conference on Recent Advances in Space Technologies (RAST)*, IEEE, pp.747–752.

[38] **Jayaram, S.** (2010). A new fast converging Kalman filter for sensor fault detection and isolation, *Sensor Review*.

[39] **Soken, H.E.**, **Hajiyev, C. and Sakai, S.i.** (2014). Robust Kalman filtering for small satellite attitude estimation in the presence of measurement faults, *European Journal of Control*, *20*(2), 64–72.

[40] **Söken, H.E. and Hajiyev, C.** (2014). REKF and RUKF for pico satellite attitude estimation in the presence of measurement faults, *Journal of Systems Engineering and Electronics*, *25*(2), 288–297.

[41] **Crassidis, J.L.** (2002). Angular velocity determination directly from star tracker measurements, *Journal of guidance, control, and dynamics*, *25*(6), 1165–1168.

[42] **Gießelmann, J.** (2006). Development of an active magnetic attitude determination and control system for picosatellites on highly inclined circular low earth orbits.

[43] **Shuster, M.D. and Oh, S.D.** (1981). Three-axis attitude determination from vector observations, *Journal of guidance and Control*, *4*(1), 70–77.

[44] **Haykin, S.** (2004). *Kalman filtering and neural networks*, volume 47, John Wiley & Sons.

[45] **Zarchan, P. and Musoff, H.** (2005). Progress in Astronautics and Aeronautics: Fundamentals of Kalman Filtering, *A Practical Approach*, *208*.

[46] **Betta, G. and Pietrosanto, A.** (2000). Instrument fault detection and isolation: State of the art and new research trends, *IEEE Transactions on Instrumentation and Measurement*, *49*(1), 100–107.

[47] **Brumback, B. and Srinath, M.** (1987). A chi-square test for fault-detection in Kalman filters, *IEEE Transactions on Automatic Control*, *32*(6), 552–554.

[48] **Rochim, A.F.R.F.** Chauvenet's Criterion, Peirce's Criterion, and Thompson's Criterion (Literatures Review).

APPENDICES

APPENDIX A: Chauvenet's Criterion

APPENDIX A

Chauvenet's Criterion

Chauvenet's criterion is a widely accepted assessment method to determine if any of the measurements from a wide set is faulty or 'bad' [48]. The method enables the detection of these faulty points through statistical approaches. Then, these faulty points can be eliminated in order to increase the reliability of the results. Beside statistical approaches, the determination of such points would not be trustworthy. The criterion suggests that all points lying outside the mean with a probability less than $1-1/2N$ should be eliminated. This indicates that the points with a probability higher than $1-1/2N$ should be considered as trustworthy. The idea is depicted below in Figure.

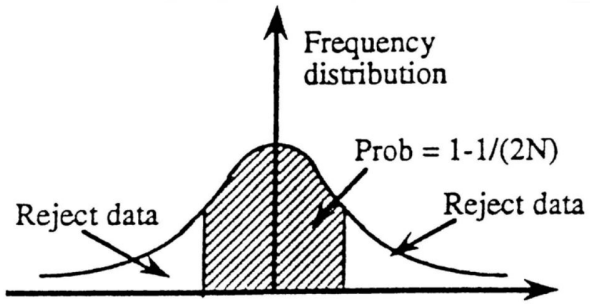

Figure A.1 : Gaussian distribution and Chauvenet's criterion.

The probability $1-1/2N$ distributed about the mean can be written in terms of a maximum deviation d_{max} from the mean value by the Gaussian probabilities given in Table 1. Then, the nondimensional maximum deviation τ_{max} can be found as follows:

$$\tau_{max} = \frac{|X_i - \bar{X}|max}{S_X} = \frac{dmax}{S_X} \qquad \textbf{(A.1)}$$

where S_X is the precision index. All data points deviating from the mean value by more than $\tau_{max}S_X$ can be eliminated. Chauvenet's criterion can be applied to a data set only once. No further applications are allowed.

Table A.1 : Chauvenet's criterion for data elimination.

Number of readings (N)	Maximum acceptable deviation (τ_{max})
3	1.38
4	1.54
5	1.65
6	1.73
7	1.80
8	1.87
9	1.91
10	1.96
15	2.13
20	2.24
25	2.33
50	2.57
100	2.81
300	3.14
500	3.29
1000	3.48
5000	3.89

CURRICULUM VITAE

Name Surname: Yeliz SAKA YILDIZ

Place and Date of Birth: Eminonu, 28/09/1992

E-Mail: sakayeliz@gmail.com

EDUCATION:

- **B.Sc.:** 2016, Istanbul Technical University, Faculty of Aeronautics and Astronautics, Astronautical Engineering Department
- **M.Sc.:** 2020, Istanbul Technical University, Aeronautics and Astronautics Engineering Program

PROFESSIONAL EXPERIENCE AND REWARDS:

- 2017-present Space Systems Engineer, Rotorbit LLC

PUBLICATIONS, PRESENTATIONS AND PATENTS ON THE THESIS:

–

OTHER PUBLICATIONS, PRESENTATIONS AND PATENTS:

- Saka, Y., Korkut, B., Paca, O., Atas, O., Ozdemir, G. T., & Yaglıoglu, B. (2019, June). Characterization of a Geostationary Satellite Thruster Plumes Using Response Surface Generation. In 2019 9th International Conference on Recent Advances in Space Technologies (RAST) (pp. 215-222). IEEE.